Alma Mater Studiorum · Università di Bologna

Scuola di Scienze
Corso di Laurea Magistrale in Fisica del Sistema Terra

Inversion of Rayleigh-wave dispersion curves using a finite-element eigenvalue/eigenvector solver, applied to the Alpine region and Italian peninsula

Relatore:	**Presentata da:**
Prof. Andrea Morelli	**Christina Tsarsitalidou**
Correlatrice:	
Dott.ssa Irene Molinari	

Sessione III
Anno Accademico 2017/2018

Abstract

The aim of this thesis is to study the inversion of Rayleigh-wave dispersion curves in order to determine the shear-wave velocity profile. This is achieved by using a set of codes in MATLAB, which perform both forward modelling and Rayleigh-wave phase velocity inversion [1]. I test two methods for retrieving shear-wave velocity structure: a perturbational approach, which is based on a finite-element method, and a nonperturbational approach, which is a direct calculation based on the Dix-type formula. The second method provides an acceptable initial model that can be further improved by the perturbational approach. First, some synthetic tests were made simulating oceanic crust. Variations on the initial model or on the thickness of the finite elements appear to have a great impact on the recovered model. In the following, the perturbational inversion is applied to the phase-velocity database constructed by seismic ambient noise from the work of Molinari et al. [2]. The data are recorded in stations all over the Italian peninsula and the Alps. The initial model used is a combination of the resulting model from the work of Molinari et al. [2] for the crustal part, and the PREM [3] for the upper-mantle part. The 3D maps of shear-wave velocity anomalies resulting from this work are further compared to the equivalent ones from the aforementioned work. This thesis is concluded with the inversion of phase-velocity data, for a few sample cases that belong to the already used database. This time, the initial model is the result of the Dix-type nonperturbational inversion [10]. This a priori model constitutes a satisfying reference model for determining 1D shear-wave velocity structure, but some restrictions might exist when using the method in order to obtain 3D structures.

Sommario

Questa tesi si pone come obiettivo lo studio del processo d'inversione nel caso di curve di dispersione delle onde di Rayleigh, con lo scopo di determinare il profilo della velocitá delle onde S. Ciò è ottenuto grazie all'uso di codici Matlab, i quali vengono impiegati sia per la risoluzione del problema diretto che per il problema inverso [1]. Ho utilizzato due diversi metodi per determinare la struttura di velocità. Il primo tipo riguarda un approccio perturbativo basato sul metodo degli elementi finiti; il secondo, è un metodo di calcolo diretto basato sulla formula di Dix ricavata dalla sismica a riflessione e costituisce un metodo non perturbativo. Quest'ultimo fornisce un modello iniziale che potrà essere in seguito ottimizzato attraverso l'approccio perturbativo. Inizialmente, test basati su dati sintetici sono stati effetuati al fine di simulare la crosta oceanica. È stato notato che eventuali variazioni al modello iniziale o variazioni allo spessore degli elementi finiti sembrano essere di grande impatto per il modello risultante. Successivamente, l'inversione perturbativa è stata applicata con dati di velocità di fase, appartenenti al database risultante dall' analisi del rumore sismico effettuata da Molinari et al. [2]. Tali dati sono stati registrati da stazioni presenti in tutto il territorio italiano e nelle Alpi. Il modello iniziale risulta da una combinazione del modello ottenuto dalla ricerca di Molinari et al. [2] e dal modello PREM [3]. In particolare, per la parte crostale è stato preso come riferimento il primo modello, per la parte riguardante il mantello superiore è stato preso in considerazione il secondo modello. Le mappe 3D di velocità di S risultanti da questo metodo vengono successivamente paragonate con le equivalenti mappe risultate dal lavoro di Molinari et al. [2]. Infine, lo stesso procedimento è stato ripetuto per un numero limitato di celle appartenenti al medesimo database. In questo caso, il modello iniziale è il modello risultante dall' inversione di Dix [10] e può essere considerato un modello di riferimento adeguato per determinare la struttura 1D delle celle prese singolarmente. Tuttavia, si riscontrerebbero alcune limitazioni nel caso in cui il metodo venisse impiegato per ottenere strutture 3D.

Acknowledgements

I would like to thank Prof. Andrea Morelli and Dr. Irene Molinari for their support and guidance during the work of the present thesis, without which this work would not have been possible. I would also like to thank my friends, both Greek and Italian, for always being there for me. Last but not least, I must express my deepest gratitude to my family, whose unwavering support and encouragement made it possible for me to get this far. To you I will be forever indebted.

Contents

Introduction **1**

I Theoretical Aspects **5**

1 Seismic Waves **7**
- 1.1 Body Waves 7
- 1.2 Surface Waves Theory 8
  - 1.2.1 Rayleigh Waves in a half-space 9
  - 1.2.2 Rayleigh waves in a layer over a halfspace 11
- 1.3 Dispersion of Surface Waves 16
  - 1.3.1 Phase and Group Velocity 16
  - 1.3.2 Dispersion Curves 17

2 Forward Study for Rayleigh waves **21**
- 2.1 Lumped Mass Method for Rayleigh Waves 21
- 2.2 Forward numerical modeling 26

3 Inverse Problem Theory **29**
- 3.1 Bayesian formulation for inverse problems 29
- 3.2 Perturbational Inversion 32
- 3.3 Nonperturbational inversion 34

II Data Analysis **37**

4 Synthetic Testing **39**
- 4.1 A short description of the Software Tools 39
  - 4.1.1 Optimal Layering 39
  - 4.1.2 Smoothness Scale 41
- 4.2 Analysis of the earth model parameters impact on dispersion curves . 42
- 4.3 Synthetic tests for the Oceanic Crust 45

5 Perturbational inversion applied to Italy **55**
- 5.1 Ambient noise database 55
- 5.2 One-Dimensional shear velocity profiles 56
- 5.3 Three-dimensional shear velocity structure 59

5.4 A priori model based on the Dix-type inversion 65

Conclusion **73**

Appendix A **79**

Bibliography **79**

List of Figures

1.1 Medium deformation when longitudinal waves propagate from left to right [4]. 8

1.2 Medium deformation transverse waves propagate from left to right [4]. 8

1.3 Deformation of the medium when Love waves propagate from left to right [4]. 9

1.4 Deformation of the medium when Rayleigh waves propagate from left to right [4]. 9

1.5 Particle motion and direction of propagation 10

1.6 Layer over a halfspace 11

1.7 (a)Dispersion curves for phase (blue) and group (black velocity data. (b) Sensitivity kernel for phase velocity. The frequency range is $0.1 - 0.65$ Hz. Low-frequency kernels are peaked in deep depths, while high-frequency kernels in shallower depths. 19

2.1 On the right: Representation of the layered system, and left: displacement and force field acting on corners between two elements . . 22

2.2 Displacements for the adjacent elements A and B 23

2.3 A schematic way to relate the matrix $[K]_j$ with $[L]_j$. The elemenents outside $[K]$ are not used. 25

2.4 Displacements for the adjacent elements A and B 26

4.1 The optimal grid vector 40

4.2 The $N \times N$ $\left|r_i - r_j\right|$ matrix; the zeros in the diagonal correspond to the each one of the N elements (layers).The arrows indicate the direction of the increasing depth (the use of the word *depth*, in the present context does not necessarily imply that the direction of the measurment is from the surface to the bottom). 41

4.3 Shear velocity variation in three different depth domains and the effect on Rayleigh phase velocity. Every couple of the subfigures correspond to an increase of the values of Vs in the domain $(0 - 24)$ km, $(24 - 150)$ km and $(150 - 400)$ km respectively. The blue dashed line indicates the variation. 43

4.4 Longitudinal velocity variation in three different depth domains and the effect on Rayleigh phase velocity.Every couple of the subfigures correspond to an increase of the values of Vp in the domain $(0 - 24)$ km, $(24 - 150)$ km and $(150 - 400)$ km respectively. The blue dashed line indicates the variation. 44

4.5 Density variation in three different depth domains and the effect on Rayleigh phase velocity. Every couple of the subfigures correspond to an increase of the values of ρ in the domain $(0-24)$ km, $(24-150)$ km and $(150-400)$ km respectively. The blue dashed line indicates the variation. 45

4.6 (a) Dispersion curves for the fundamental and first overtone data (blue), initial model (red) and predicted data from the inversion (black). (b) Shear-wave velocity profile for true model(blue), initial model (red dashed, which is the polynomial fit of the green) and the last update of the inversion (black). (c) Sensitivity kernels for the fundamental mode and first overtone. The frequency range is (0.001-0.781) Hz. 49

4.7 (a) Dispersion curves for the fundamental and first overtone data (blue), initial model (red) and predicted data from the inversion (black). (b) Shear-wave velocity profile for true model(blue), initial model (red dashed, which is the polynomial fit of the green) and the last update of the inversion (black). (c) Sensitivity kernels for the fundamental mode and first overtone. The frequency range is (0.001-0.781) Hz. 50

4.8 (a) Dispersion curves for the fundamental and first overtone data (blue), initial model (red) and predicted data from the inversion (black). (b) Shear-wave velocity profile for true model(blue), initial model (red dashed, which is the polynomial fit of the green) and the last update of the inversion (black). (c) Sensitivity kernel for the fundamental mode. The frequency range is (0.02-0.26) Hz. 51

4.9 (a) Dispersion curves for the fundamental and first overtone data (blue), initial model (red) and predicted data from the inversion (black). (b) Shear-wave velocity profile for true model(blue), initial model (red dashed, which is the polynomial fit of the green) and the last update of the inversion (black). (c) Sensitivity kernel for the fundamental mode. The frequency range is (0.02-0.26) Hz. 52

4.10 (a) Dispersion curves for the fundamental data (blue), initial model (red) and predicted data from the inversion (black). (b) Shear-wave velocity profile for true model(blue), initial model (red dashed, which is the polynomial fit of the green) and the last update of the inversion (black). (c) Sensitivity kernel for the fundamental mode. The curves correspond to 3 s, 4 s, 5 s, 6 s, 7 s, 9 s, 13 s, 21 s, 50 s from shallow to deep depths. 53

4.11 (a) Dispersion curves for the fundamental data (blue), initial model (red) and predicted data from the inversion (black). (b) Shear-wave velocity profile for true model(blue), initial model (red dashed, which is the polynomial fit of the green) and the last update of the inversion (black). (c) Sensitivity kernel for the fundamental mode. The curves correspond to 3 s, 4 s, 5 s, 6 s, 7 s, 9 s, 13 s, 21 s, 50 s from shallow to deep depths. 54

5.1 Stations where the seismograms were recorded.(After Molinari et al. [2]) 56
5.2 (a) Dispersion curves for the fundamental mode data (blue), initial model (red) and predicted data from the inversion (black). (b) Shear-wave velocity profile for true model(blue), initial model (red dashed, which is the preferred model in figure 5 of Molinari's et al. work [2]) and the last update of the inversion (black). (c) Sensitivity kernel for the fundamental mode. (Northern Alpine foreland case) 58
5.3 (a) Dispersion curves for the fundamental mode data (blue), initial model (red) and predicted data from the inversion (black). (b) Shear-wave velocity profile for true model(blue), initial model (red dashed, which is the preferred model in figure 5 of Molinari's et al. work [2]) and the last update of the inversion (black). (c) Sensitivity kernel for the fundamental mode. (Alpine orogen crust case) 59
5.4 Shear velocity maps at depths (a)3 km (b) 4 km (c) 7 km and 10 km. 62
5.5 Shear velocity maps at depths (a)20 km (b) 22 km (c) 29 km and 36 km. 63
5.6 Vertical section starting from central Italy (B) up to South Germany (A). The distance is about 700 km. (1°corresponds to 96 km) 64
5.7 The two points A and B that set the limits to the vertical section presented in 5.6. 64
5.8 Sample cells in Nothern Alpine, that was made the pertubational and nonperturbational inversion. 66
5.9 Nothern Alpine foreland (C) 68
5.10 South-West Alpine foreland (D) 70
5.11 Alpine Orogen crust(E) 71

Introduction

Surface waves are the large-amplitude long-period waves that appear on a seismogram after the P-wave and S-wave arrival. Their energy is concentrated in the Earth surface and decays slower than the energy of the body waves. The two main types of surface waves are the Rayleigh and the Love waves.

Rayleigh waves constitute a powerful tool for the study of the subsurface properties due to their dispersive character, the fact that their velocity is a function of frequency. Velocity variations depend on the depth domain sampled by each frequency. High frequencies sample the shallow structure, while low frequencies are more sensitive to deeper structures. Measuring the surface wave dispersion along different earthquake-receiver paths, or between two receivers in case of ambient noise data, allows us to investigate the structure beneath and between the two points. In other words, dispersion data received from different locations are used in tomographic inversion to visualize the distribution of phase or group velocity within the defined area. Following this, the profile of the Earth model parameters (P-wave velocity, S-wave velocity, density) at any point can be inferred by its dispersion curve.

Consequently, inversion of dispersion curves for the determination of those model parameters remains an important task to solve.

Although Rayleigh waves are depended on all model parameters, not all of them contribute with the same manner to the dispersion curve. If a variation of a specific parameter in a certain frequency range does not provide significant variation on the dispersion curve, then that parameter is not worth being inverted. As addressed by Xia [5], Rayleigh waves are mainly influenced by near-surface shear-wave velocity and so, this is usually the model parameter determined by the inversion process.

The scope of the present thesis, is to study and improve the method of Rayleigh-wave dispersion curves inversion in order to obtain reliable shear-wave velocity profiles. I follow the new approach presented by Haney and Tsai, 2017 [1], which consists of two different inversion methods: a perturbational method based on finite elements and a nonperturbational method developed on the Dix formula. If compared with the usual approach to retrieve the shear-wave velocity profile from dispersion, this one presents the advantage of facing the forward problem as a simple eigenvalue/eigenvector problem, which can be solved numerically by already established codes. An other advantage is that the nonperturbational method can be used in order to obtain an acceptable initial model, wherever there is lack of a priori information. The thesis consists of two parts: the first part is focused on the theoretical aspects of the forward and inverse problem, when working with Rayleigh-wave measurements. The second part treats the modelling and inversion of both synthetic and real dispersion curves.

The forward problem of calculating dispersion curves from a 1D structural model is based on the finite-element method of Lysmer [6]. The medium is represented by finite rectangular elements, in the corners of which the mass exists. This method does not use the displacement potentials for the formulation of the problem, but with an appropriate representation of the continuous layered system, leads to an eigenvalue/eigenvector problem to be solved. The advantages of this method are the accuracy, since the layers are thinner with respect to the wavelength, and more importantly, its direct link with the inverse problem, due to the matrix formulation of the forward problem.

With this approach, the inverse problem constitutes an extension of the forward problem, when calculating the perturbation in phase or group velocity caused by perturbations in the material properties. Over a wide range of frequencies, phase or group velocity can be expressed in terms of perturbations in material properties, using the appropriate sensitivity kernels, whose formulation will be shown in section 3.2. To express the aforementioned relation in terms of the perturbed shear-wave velocity, either the Poisson's ratio and the density or the longitudinal velocity and the density have to be considered fixed for the inversion process. By assuming constant one of these two pairs of parameters, I obtain a relation between the perturbations of phase and shear-wave velocity, and so I can proceed with the inversion for the depth-dependent shear-wave velocity profile. Whatever the case may be, a linear relation for the perturbed phase or group velocity and the perturbed shear-wave velocity is found, related by the equivalent kernel, which is a weighted sum of the kernel properties. The inversion method is based on the algorithm of total inversion [7], and the solution is regularized on the basis of weighted-damped least squares.

The second part of this work consists of synthetic tests and an application to real dispersion curves, as described in Chapter 4 and 5, respectively.

In the first section of Chapter 4 are presented the contributions of S-wave velocity, P-wave velocity and density to the Rayleigh-wave phase velocity over a wide frequency range.

Following this simple forward problem test, I present a series of tests simulating the oceanic crust. This is the case whenever applying surface-wave inversion with ocean bottom seismometers [8]. In this case the initial model is a smooth rapresentation of CRUST 1.0 [9], for the chosen cell. The tests consist of variations in the frequency range, in the thickness of the layered system and in the initial model. In some cases fundamental mode and first overtone phase velocities are jointly inverted.

In the last Chapter, the linearized inversion is applied to the ambient noise database from the work of Molinari et al.[2]. Ambient seismic noise is mainly dominated by surface waves, and with the appropriate data processing, one can obtain information on the propagation properties of the wavefield [26]. Cross-correlation is applied to the vertical component of the seismic records from pairs of stations, and with the two-station method the phase-velocity is obtained. The initial model, that I use, for the crustal part is the average of the 500 best-fitting models, resulting from the inversion of the same work. The upper-mantle parameter values are equal to the PREM model values. Initially, the code is tested to the fundamental mode phase velocity data for a few sample cells in Northern Alpine and so, the 1D shear-wave velocity structure is obtained. Next, the inversion is applied to data obtained all over the Italian peninsula and the Alps. The database is dense enough to construct the 3D shear-wave velocity maps over the entire region. The differences in shear-wave velocity structure between the different existent types of crust (oceanic crust, foreland basin, orogen crust) are well-imaged for different depth domains. The 3D maps obtained by the linearized inversion are consistent with the maps of the work of Molinari et al. [2], wherever exists sufficient resolution. This kind of study has a vital role for the better understanding of the evolution of the lithosphere in complex earth structures, like the ones existent around the Mediterranean region.

In the concluding part of the thesis, the inversion method is repeated to dispersion curves for some sample cells, that belong to the same database as before, but this time a different a priori model is used. This particular initial model is the result of a nonperturbational inversion method [10] applied to the same data that are subsequently inverted following the perturbational theory. The idea behind the aforementioned inversion originates from the Dix formula, often applied in reflection seismology: in a series of flat, parallel layers the stacking velocity of a layer equals the root mean square (rms) velocity of the layers that overlay the inteface of that layer, weighted by traveltimes. Surface wave velocity can be considered as the stacking velocity and shear-wave velocity as the interval velocity. The Dix-type inversion can be made by assuming propagating Rayleigh waves mapped by different cases of the shear-wave profile. In order to seek the best choice of the nonperturbational inversion parameters, the resulting 1D shear-wave velocity structure is compared with the best solution model [2].

Part I

Theoretical Aspects

Chapter 1

Seismic Waves

In physics there are two kinds of waves, *progressive* and *standing.* Seismic waves are also divided into these two categories. Progressive elastic waves travel away from the seismic source and through the layers of the Earth. Standing waves, also known as Earth's free oscillations, can be imagined as vibrations produced by large earthquakes.

The two principal types of progressive elastic waves, according to the spatial concentration of energy, are the *body waves*, which propagate in the interior of the medium and the *surface waves*, concentrated at the surface. The latter can be divided into *longitudinal* and *transverse waves* and *Rayleigh* and *Love waves*, respectively.

Studying the body waves has probably provided with the most important information about the constitution of the Earth's interior [11]. The structure of the crust, mantle and core is the result of body wave studies.

Surface waves studies are important as well. They usually have the largest amplitude on a seismogram, and can contribute greatly to the damaging effects that an earthquake might produce. In addition to this, problems such as the existence and structure of the low-velocity zone between the lithosphere and the asthenosphere in the upper mantle, the discrimination between continental and oceanic crust, the determination of the crustal properties and its lateral inhomogeneities can be faced by studying the surface waves.

In this work, I will only deal with Rayleigh wave. The physics and the main properties of this kind of waves are introduced in the following paragraphs, framed in a greater theoretical context of wave propagation.

1.1 Body Waves

As already mentioned, body waves are of two types:

1) Longitudinal waves, also called P (primary) waves, since they are the first to appear on seismograms. During propagation, they cause the compression and rarefaction of the material, not the rotation, and every particle moves from its equilibrium position following the direction of the wave.

2) Transverse waves, also called in seismology S (secondary) waves. In contrast to the P waves, the S waves cause the shearing and rotation of the material. The

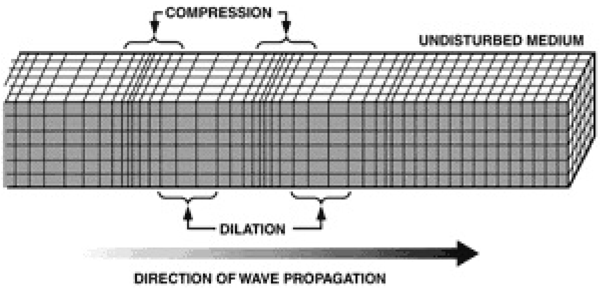

Figure 1.1: Medium deformation when longitudinal waves propagate from left to right [4].

particles move in direction perpendicular to the direction of the wave propagation and there is no volume change.

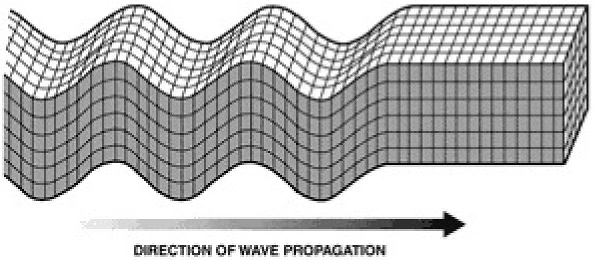

Figure 1.2: Medium deformation transverse waves propagate from left to right [4].

For a homogeneous and isotropic medium the velocity of the P waves, α, and the S waves, β, is given by the following formulas

$$\alpha = \sqrt{\frac{\lambda + 2\mu}{\rho}}, \ \beta = \sqrt{\frac{\mu}{\rho}},$$

where μ, the shear modulus, and λ are the Lamé coefficients and ρ the density. For $\lambda = \mu$, Poisson's relation, we obtain

$$\alpha = \beta\sqrt{3},$$

an often used simplification in seismology.

An important difference between the two types of waves is that, although they both propagate into solid, only P waves propagate to liquid and gas, where $\mu = 0$.

1.2 Surface Waves Theory

In a finite extent, or *bounded*, medium the surface waves are *guided* along its surface. They are high amplitude, long-period waves that appear in a seismogram after the P and S waves. There are two types of surface waves:

1) Love waves, which are the trapped *SH* waves near the surface of the Earth. They are horizontally polarized and provoke the transverse particle motion, parallel to the surface of the medium. Love waves, in contrast to the Rayleigh waves, cannot propagate in a homogeneous half-space. The simplest medium structure, in which

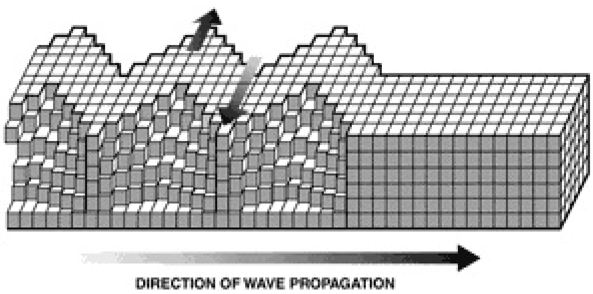

Figure 1.3: Deformation of the medium when Love waves propagate from left to right [4].

these waves can travel, can be when a homogeneous isotropic layer resides in a homogeneous isotropic half-space.

2) Rayleigh waves, which represent the result of the interaction of the P and SV waves. They are elliptically polarized in a plane vertical to the surface and parallel to the direction of motion. In the next section, I will discuss in detail the properties and the physics of these waves.

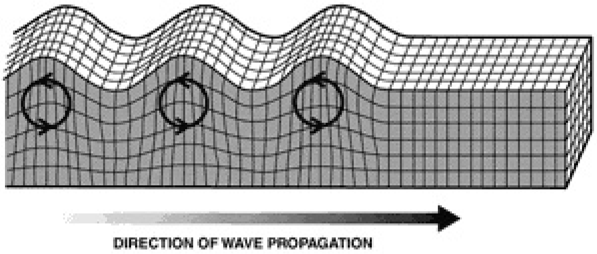

Figure 1.4: Deformation of the medium when Rayleigh waves propagate from left to right [4].

An important characteristic of the surface waves, useful for my purpose, is the *dispersion*: the fact that the velocity is a function of frequency. Surface wave arrivals break up, or *disperse*, as they propagate away from the source: a sequence of wave arrivals is created, depending on each wave frequency. This phenomenon is greatly used in order to study the structure of the medium, which the waves have passed through.

In the following, I will describe the important theoretical characteristics of the Rayleigh waves which are important for the main part of this work.

1.2.1 Rayleigh Waves in a half-space

The simplest medium structure in which the existence of the Rayleigh waves can be studied is a homogeneous isotropic half-space with a free surface. By following the Stein and Wysession [12], I will present the related formulation.

First of all, a Cartesian coordinate system is defined with its (x,y) plane being parallel to the surface of the medium and z axis being equal to 0 in the free surface and positive into the medium.

Since Rayleigh waves is the combination of the P and SV waves, I shall write their potentials respectively

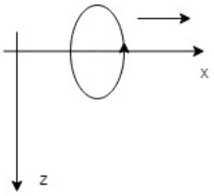

Figure 1.5: Particle motion and direction of propagation

$$\phi = Ae^{-ik_x rz} e^{i(\omega t - k_x x)} \tag{1.1}$$
$$\psi = Be^{-ik_x sz} e^{i(\omega t - k_x x)} \tag{1.2}$$

where ω is the frequency, k_x the x component of the wave-number, A and B the amplitudes, $r = (\frac{c_x^2}{\alpha^2} - 1)^{\frac{1}{2}}$ and $s = (\frac{c_x^2}{\beta^2} - 1)^{\frac{1}{2}}$, with c_x being the so-called apparent velocity along the x-axis.

In order to proceed, the appropriate boundary conditions must be derived. The nature of the surface-wave problem requires energy to be trapped near the surface. Consequently, the energy cannot propagate at large distances, while the free-surface condition is still valid.

For the first boundary condition to be satisfied, I must impose decaying displacement away from the surface, as $z \longrightarrow \infty$. That means that the equations for r and s will take the following form:

$$r = -i(1 - \frac{c_x^2}{\alpha^2})^{\frac{1}{2}}, s = -i(1 - \frac{c_x^2}{\beta^2})^{\frac{1}{2}},$$

as it is required for the c_x to be less than the shear-wave velocity β.

For the free-surface boundary condition, I apply zero stress components, $\tau_{zx} = \tau_{zz} = 0$ for $z = 0$. After expressing the stress components in terms of the potentials and substituting appropriately for this problem, I obtain:

$$\tau_{zx}(x, 0, t) = 0 = 2rA + (1 - s^2)B \tag{1.3}$$
$$\tau_{zz}(x, 0, t) = 0 = [\lambda(1 + r^2) + 2\mu r^2]A + 2\mu sB, \tag{1.4}$$

where λ and μ are the Lamé coefficients.

The next step is expressing the 1.3 and 1.4 in terms of the velocities α, β and c_x, so as to obtain the following system for A and B,

$$2(\frac{c_x^2}{\alpha^2} - 1)^{\frac{1}{2}} A + (2 - \frac{c_x^2}{\beta^2})B = 0 \tag{1.5}$$
$$(\frac{c_x^2}{\beta^2} - 2)A + 2(\frac{c_x^2}{\beta^2} - 1)^{\frac{1}{2}} B = 0 \tag{1.6}$$

and find the c_x velocity formula for the Rayleigh waves in a half-space.

I obtain the non-trivial solution of the system by setting its determinant equal to zero,

$$(2 - \frac{c_x^2}{\beta^2})^2 + 4(\frac{c_x^2}{\beta^2} - 1)^{\frac{1}{2}}(\frac{c_x^2}{\alpha^2} - 1)^{\frac{1}{2}} = 0. \tag{1.7}$$

Considering a Poisson solid, the velocities α and β, satisfy the relation $\frac{\alpha^2}{\beta^2} = 3$, and so the previous equation takes the below form

$$(\frac{c_x^2}{\beta^2})[\frac{c_x^6}{\beta^6} - 8\frac{c_x^4}{\beta^4} + (\frac{56}{3})\frac{c_x^2}{\beta^2} - \frac{32}{3}] = 0. \tag{1.8}$$

After rejecting the trivial solution of $\frac{c_x^2}{\beta^2} = 0$, which describes a static situation, and since the term in square brackets is a third degree polynomial in $\frac{c_x^2}{\beta^2}$, I expect four roots and accept only those which are less than 1 (trapped waves, $c_x < \beta$).

And so, the apparent velocity of Rayleigh waves for a homogeneous half-space, which is also a Poisson solid, is

$$c_x = 0.92\beta.$$

Substituting this result to the equations of the potentials 1.1 and then solving for the equations of the displacement for x and z components, will provide information about the polarization of the Rayleigh waves. When they propagate in the $+x$ direction, the particle motion is a retrograde ellipse.

The demonstration just illustrated describes a particular case of the surface waves, the non-dispersive one. Although highly didactic, considering the Earth as a homogeneous half-space is not realistic and so, the investigation of problems representing more complicated media and structures is of high priority in Geophysics. The Rayleigh waves in such media are dispersive, as will be discussed in detail in the next section.

1.2.2 Rayleigh waves in a layer over a halfspace

The problem of Rayleigh-wave propagation in a layer over a half-space represents a simple but still quite realistic case in the Earth and it is quite simple to algebraically solve the equation of motion. The properties and physics of the Rayleigh waves propagating in such media will be investigated in detail, by following Novotný [13].

Let's consider the structure presented in figure 1.6. The parameters are the same as in the previous section, with the only difference the index 1 and 2, which refers to the layer and half-space, respectively. In addition to this, I will assume that the layer thickness is equal to H and that $\alpha_1 < \alpha_2$ and $\beta_1 < \beta_2$.

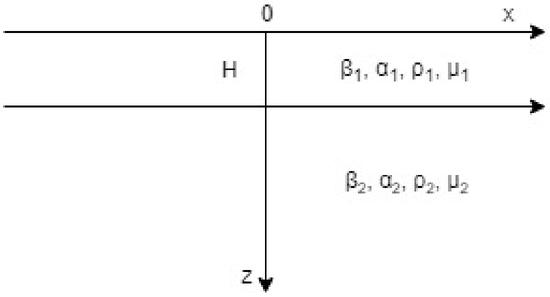

Figure 1.6: Layer over a halfspace

A harmonic plane wave is propagating along the x-axis with a phase velocity c, an angular frequency ω and polarization plane the (x, z). Then, the displacement vector can be written as,

$$\mathbf{u_m} = (u_m, 0, w_m), m = 1, 2 \tag{1.9}$$

with no dependence of the y coordinate.

In order to solve for the displacement field, I should seek for the potentials, as the first can be described in terms of the second by the following relations,

$$u_m = \frac{\partial \phi_m}{\partial x} - \frac{\partial \psi_m}{\partial z}, w_m = \frac{\partial \phi_m}{\partial z} + \frac{\partial \psi_m}{\partial x}. \tag{1.10}$$

The potentials, represented in this case, take the form

$$\phi_m(x, z, t) = f_m(z) e^{i\omega(t - \frac{x}{c})}, \psi_m(x, z, t) = g_m(z) e^{i\omega(t - \frac{x}{c})}, \tag{1.11}$$

where the velocity c is the same in both media and for both potentials.

The 1.11 must satisfy the wave equations,

$$\nabla^2 \phi_m = \frac{1}{\alpha_m^2} \frac{\partial^2 \phi_m}{\partial t^2}, \nabla^2 \psi_m = \frac{1}{\beta_m^2} \frac{\partial^2 \psi_m}{\partial t^2}, \tag{1.12}$$

from which, after omitting some simple algebraic calculations, we may obtain the following expression for $f_m(z)$ and $g_m(z)$,

$$f_m(z) = a_m^- e^{ikr_m z} + a_m^+ e^{-ikr_m z},\ g_m(z) = b_m^- e^{iks_m z} + b_m^+ e^{-iks_m z}, \tag{1.13}$$

where $k = \frac{\omega}{c}$, r_m and s_m are the characteristic lengths defined in 1.2.1, and $a_m^{+,-}$, $b_m^{+,-}$ are arbitrary constants.

For the energy to be trapped near the surface of the layer, I must again assume that

$$r_2 = i(1 - (\frac{c}{\alpha_2})^2)^{\frac{1}{2}},\ s_2 = i(1 - (\frac{c}{\beta_2})^2)^{\frac{1}{2}},$$

and so, $c < \beta_2 < \alpha_2$. In addition to this, we must also impose $a_2^+ = b_2^+ = 0$ because increasing exponentially terms in the half-space cannot exist.

At this point, and after writing the formulas 1.13 in a more convenient way, we get

$$\begin{aligned} f_1(z) &= A \cos kr_1 z + B \sin kr_1 z,\ f_2(z) = C e^{ikr_2(z-H)} \\ g_1(z) &= D \cos ks_1 z + E \sin ks_1 z,\ g_2(z) = F e^{iks_2(z-H)}. \end{aligned} \tag{1.14}$$

The constants in the 1.14 are equal to

$$\begin{aligned} A = a_1^- + a_1^+,\ B = i(a_1^- - a_1^+),\ C = a_2^- e^{ikr_2 H} \\ D = b_1^- + b_1^+,\ E = i(b_1^- - b_1^+),\ F = b_2^- e^{iks_2 H} \end{aligned} \tag{1.15}$$

Substituting in 1.11 will give the following relations for the layer and the halfspace,

$$\begin{aligned} \phi_1 &= (A \cos \xi + B \sin \xi) e^{i(\omega t - kx)},\ \phi_2 = C e^{-\zeta} e^{i(\omega t - kx)} \\ \psi_1 &= (D \cos \eta + E \sin \eta) e^{i(\omega t - kx)},\ \psi_2 = F e^{-\chi} e^{i(\omega t - kx)} \end{aligned} \tag{1.16}$$

where $\xi = kr_1 z$, $\eta = ks_1 z$, $\zeta = -ikr_2(z-H)$, $\chi = -iks_2(z-H)$.

After differentiating the potentials, which are given by 1.16, according to the 1.10, I obtain the formulas for the corresponding displacements,

$$\begin{gathered} u_1 = -k[i(A\cos\xi + B\sin\xi) + s_1(-D\sin\eta + E\cos\eta)],\ u_2 = -ik(Ce^{-\zeta} + s_2Fe^{-\chi}), \\ w_1 = -k[r_1(A\sin\xi - B\cos\xi) + i(D\cos\eta + E\sin\eta)],\ w_2 = ik(r_2Ce^{-\zeta} - F^{-\chi}). \end{gathered} \tag{1.17}$$

I will use the same expressions for the potential, in 1.16, to find the stress components, whose general formulas for the $P-SV$ problems are

$$\begin{gathered} \tau_{zx} = \mu\left(2\frac{\partial^2\phi}{\partial x\partial z} + \frac{\partial^2\psi}{\partial x^2} - \frac{\partial^2\psi}{\partial z^2}\right), \\ \tau_{zz} = \frac{\lambda}{\alpha^2}\frac{\partial^2\phi}{\partial t^2} + 2\mu\left(\frac{\partial^2\phi}{\partial z^2} + \frac{\partial^2\psi}{\partial x\partial z}\right), \\ \tau_{zy} = 0. \end{gathered} \tag{1.18}$$

So, substituting the 1.16 into the 1.18 will give

$$\begin{gathered} \left(\tau_{zx}\right)_1 = \rho_1\omega^2[i\gamma_1r_1(A\sin\xi - B\cos\xi) - \delta_1(D\cos\eta + E\sin\eta)], \\ \left(\tau_{zz}\right)_1 = \rho_1\omega^2[\delta_1(A\cos\xi + B\sin\xi) + i\gamma_1s_1(D\sin\eta - E\cos\eta)], \\ \left(\tau_{zx}\right)_2 = \rho_2\omega^2(\gamma_2r_2Ce^{-\zeta} - \delta_2Fe^{-\chi}), \\ \left(\tau_{zz}\right)_2 = \rho_2\omega^2(\delta_2Ce^{-\zeta} + \gamma_2s_2Fe^{-\chi}), \end{gathered} \tag{1.19}$$

with $\gamma_m = 2(\frac{\beta_m}{c})^2$ and $\delta_m = \gamma_m - 1$.

Undoubtedly, I need to determine the six unknown constants, from A to F. This will occur after considering the appropriate boundary conditions at the free surface and at the discontinuity created between the layer and the half-space.

The first one requires zero stresses at the free surface,

$$\left(\tau_{zx}\right)_1 = 0,\ \left(\tau_{zz}\right)_1 = 0\, for\, z = 0$$

while the second one demands the continuity for both displacement and stress field at the interface,

$$u_1 = u_2,\ w_1 = w_2,\ \left(\tau_{zx}\right)_1 = \left(\tau_{zx}\right)_2,\ \left(\tau_{zz}\right)_1 = \left(\tau_{zz}\right)_2 for\, z = H.$$

The use of the boundary conditions leads to the following system of six homogeneous equations in six unknown constants, A to F,

$$\begin{gathered} i\gamma_1r_1B + \delta_1D = 0, \\ \delta_1A - i\gamma_1s_1E = 0, \\ i(A\cos P + B\sin P) - s_1(D\sin Q - E\cos Q) - iC - is_2F = 0, \\ r_1(A\sin P - B\cos P) + i(D\cos Q + E\sin Q) + ir_2C - iF = 0, \\ i\gamma_1r_1(A\sin P - B\cos P) - \delta_1(D\cos Q + E\sin Q) - \rho\gamma_2r_2C + \rho\delta_2F = 0, \\ \delta_1(A\cos P + B\sin P) + i\gamma_1s_1(D\sin Q - E\cos Q) - \rho\delta_2C - \rho\gamma_2s_2F = 0. \end{gathered} \tag{1.20}$$

Please note that the first two equations come from the implementation of the first boundary condition into the first two expressions of the 1.19, while the rest of them come from applying the second boundary condition into the 1.17 and 1.19.

For the sake of simplicity, I have substituted with $P = kr_1H$, $Q = ks_1H$ and $\rho = \frac{\rho_1}{\rho_2}$.

To have a non-trivial solution of the linear system in 1.20 I need to set its determinant equal to zero. In this case, I obtain the dispersion equation for the unknown phase velocity c.

Solutions obtained directly by solving for the condition that the sixth order determinant equals zero can be found in the literature. However, in this work following Novotný [13], I will try to solve a lower order determinant by reducing the number of equations of the system 1.20 from six to four.

In order to do so, I modify properly the first two equations of the system 1.20 with the purpose of eliminating the constants B and E from the rest of them.

So, if

$$B = i\frac{G}{r_1}D,\ E = -i\frac{G}{s_1}A,\ with\, G = \frac{\delta_1}{\gamma_1}$$

then, the new expression of the dispersion equation will be the third-order determinant of the following four equations system,

$$\begin{aligned} iA(\cos P - G\cos Q) - D(Gr_1^{-1}\sin P + s_1\sin Q) - iC - is_2F = 0, \\ A(r_1\sin P + Gs_1^{-1}\sin Q) - iD(G\cos P - \cos Q) + ir_2C - iF = 0, \\ iA(\gamma_1 r_1\sin P + \delta_1 Gs_1^{-1}\sin Q) + \delta_1 D(\cos P - \cos Q) - \rho\gamma_2 r_2 C + \rho\delta_2 F = 0, \\ A\delta_1(\cos P - \cos Q) + iD(\delta_1 Gr_1^{-1}\sin P + \gamma_1 s_1\sin Q) - \rho\delta_2 C - \rho\gamma_2 s_2 F = 0. \end{aligned} \tag{1.21}$$

Multiplying the second and the forth of the equations 1.21 by i and $-i$ respectively, will define two new unknowns, $\widetilde{A} = iA$ and $\widetilde{C} = -iC$. If the determinant of the system for the unknowns $\widetilde{A}$, D, $\widetilde{C}$ and F equals zero, the non-trivial solution will be found,

$$\begin{vmatrix} \cos P - G\cos Q & -Gr_1^{-1}\sin P - s_1\sin Q & 1 & -is_2 \\ r_1\sin P + Gs_1^{-1}\sin Q & G\cos P - \cos Q & -ir_2 & 1 \\ \gamma_1 r_1\sin P + \delta_1 Gs_1^{-1}\sin Q & \delta_1(\cos P - \cos Q) & -ir_2\rho\gamma_2 & \rho\delta_2 \\ -\delta_1(\cos P - \cos Q) & \delta_1 Gr_1^{-1}\sin P + \gamma_1 s_1\sin Q & -\rho\delta_2 & i\rho\gamma_2 s_2 \end{vmatrix} = 0 \tag{1.22}$$

By using the Laplace Expansion Theorem, the determinant 1.22 is represented by

$$L_1H_1 + L_2H_2 + L_3H_3 + L_4H_4 + L_5H_5 + L_6H_6 = 0, \tag{1.23}$$

where L_1 to L_6 are the six minors of the second-order derived by the first two columns of the 1.22 and H_1 to H_6 the equivalent co-factors formulated by the last two columns of the aforementioned. This particular development is chosen due to the fact that the first two columns represent the quantities of the layer, while the last two columns represent the quantities of the half-space.

In particular, and if a_{ij} is the element in the i-th row and j-th column of the matrix in 1.22, we calculate the minors

$$\begin{aligned}
L_1 &= \begin{vmatrix} a_{11} & a_{12} \\ a_{21} & a_{22} \end{vmatrix} = 2G - (1+G^2)\cos P \cos Q + r_1 \sin P s_1 \sin Q + G^2 r_1^{-1} \sin P s_1^{-1} \sin Q, \\
L_2 &= \begin{vmatrix} a_{11} & a_{12} \\ a_{31} & a_{32} \end{vmatrix} = \delta_1[(1+G)(1-\cos P \cos Q) + G^2 r_1^{-1} \sin P s_1^{-1} \sin Q] + \gamma_1 r_1 \sin P s_1 \sin Q, \\
L_3 &= \begin{vmatrix} a_{11} & a_{12} \\ a_{41} & a_{42} \end{vmatrix} = \cos P s_1 \sin Q + G^2 \cos Q r_1^{-1} \sin P, \\
L_4 &= \begin{vmatrix} a_{21} & a_{22} \\ a_{31} & a_{32} \end{vmatrix} = G^2 \cos P s_1^{-1} \sin Q + \cos Q r_1 \sin P, \\
L_5 &= \begin{vmatrix} a_{21} & a_{22} \\ a_{41} & a_{42} \end{vmatrix} = L_2, \\
L_6 &= \begin{vmatrix} a_{31} & a_{32} \\ a_{41} & a_{42} \end{vmatrix} = \delta_1^2[2(1-\cos P \cos Q) + G^2 r_1^{-1} \sin P s_1^{-1} \sin Q] + \gamma_1^2 r_1 \sin P s_1 \sin Q.
\end{aligned} \tag{1.24}$$

For the co-factors, I have respectively

$$\begin{aligned}
H_1 &= \begin{vmatrix} a_{33} & a_{34} \\ a_{43} & a_{44} \end{vmatrix} = \rho^2(\delta_2^2 + \gamma_2^2 r_2 s_2), \\
H_2 &= -\begin{vmatrix} a_{23} & a_{24} \\ a_{43} & a_{44} \end{vmatrix} = -\rho(\delta_2 + \gamma_2 r_2 s_2), \\
H_3 &= \begin{vmatrix} a_{23} & a_{24} \\ a_{33} & a_{34} \end{vmatrix} = i\rho r_2, \\
H_4 &= \begin{vmatrix} a_{13} & a_{14} \\ a_{43} & a_{44} \end{vmatrix} = i\rho s_2, \\
H_5 &= -\begin{vmatrix} a_{13} & a_{14} \\ a_{33} & a_{34} \end{vmatrix} = H_2 \\
H_6 &= \begin{vmatrix} a_{13} & a_{14} \\ a_{23} & a_{24} \end{vmatrix} = 1 + r_2 s_2.
\end{aligned} \tag{1.25}$$

Please note that, in order to be a co-factor, a minor has to be multiplied by $(-1)^{i+j+k+l}$, where i, j, k, l represent the corresponding rows and vectors. That is why there is a $-$ sign in H_2 and H_5.

Finally, if I substitute $L_5 = L_2$ and $H_5 = H_2$ into the dispersion equation 1.23, I obtain

$$L_1H_1 + 2L_2H_2 + L_3H_3 + L_4H_4 + L_6H_6 = 0, \tag{1.26}$$

which is rather simple. Furthermore, for the simplification and calculation of the minors, some trigonometric properties can be taken into considerations, such as $\cos^2 x + \sin^2 x = 1$.

One can follow a similar treatment for the case of Rayleigh waves in a multilayer medium, which constitutes the representation of the system divided in n discrete layers, together with the equivalent boundary conditions.

1.3 Dispersion of Surface Waves

Dispersion of waves can be of two types:

- material or physical dispersion and
- geometrical dispersion.

The *material dispersion*, as its name indicates, is closely related to the nature and the physical properties of the material, or medium, in which the waves propagate. In the case of the Earth, the material dispersion causes the attenuation of the elastic waves.

On the other hand, the *geometrical dispersion* is the result of the interference of waves. This is the kind of dispersion that happens to waves, when they propagate to media with complicated structure. It is easy to understand why geometrical dispersion is frequently studied for surface waves.

1.3.1 Phase and Group Velocity

The dispersion of surface waves is related to the dependence of the *phase* velocity on frequency. Consequently, surfaces wave propagation is characterised by frequency-dependent *phase* and *group* velocities.

In order to study their difference, I will first express the displacement field $u(x,t)$ as an integral over harmonic plane waves of all frequencies ω,

$$u(x,t) = \int A(\omega) \exp i[\omega t - k(\omega)x + \phi(\omega)]d\omega, \tag{1.27}$$

where the wavenumber $k(\omega)$ and the amplitude $A(\omega)$ depends on the angular frequency ω. The argument of the exponential function in 1.27 consists of two terms, $\omega t - k(\omega)x$ and $\phi(\omega)$. From the first term I can define the phase velocity

$$c(\omega) = \frac{\omega}{k(\omega)} \tag{1.28}$$

for every angular frequency.

The second term, $\phi(\omega)$, can be interpreted as the initial phase of the wave when it was generated.

The individual harmonic waves that produce the displacement in 1.27 propagate with different phase velocities $c(\omega)$, which will also be different from the velocity of the wave packet.

In order to express the displacement both in terms of phase and group velocity, which actually represents the velocity of the propagation of energy, we expand the wavenumber $k(\omega)$ about ω_0 in Taylor series,

$$k(\omega) = k(\omega_0) + \left.\frac{dk}{d\omega}\right|_{\omega_0} (\omega - \omega_0) \tag{1.29}$$

and substitute it to the 1.27. I obtain

$$u(x,t) = \int_{\omega_0 - d\omega}^{\omega_0 + d\omega} A(\omega) \exp\left[i\big((\omega - \omega_0)\big(t - \left.\frac{dk}{d\omega}\right|_{\omega_0} x\big) + (\omega_0 t - k(\omega_0)x) + \phi(\omega)\big)\right] d\omega. \tag{1.30}$$

The first two terms of the exponential correspond to propagating waves with different velocities. The term $(\omega_0 t - k(\omega_0)x)$ describes the propagation of the carrier wave at frequency ω_0 with velocity $c(\omega_0) = \frac{\omega_0}{k(\omega_0)}$. The term $\big(t - \left.\frac{dk}{d\omega}\right|_{\omega_0} x\big)$ describes a slowly varying envelope that propagates with a velocity $U(\omega_0) = \left.\frac{d\omega}{dk}\right|_{\omega_0}$.

It is straightforward to show that by expanding for a wide frequency band will give the group velocity as a function of angular frequency,

$$U(\omega) = \frac{d\omega}{dk}. \tag{1.31}$$

The phase and group velocities are related to

$$U = c + k\frac{dc}{dk} \tag{1.32}$$

or in terms of wavelength

$$U = c - \lambda\frac{dc}{d\lambda}. \tag{1.33}$$

Note that for a non-dispersive wave the group velocity equals the phase velocity.

In general, for a typical Earth profile the phase velocity is always faster than the group velocity, and increases monotonically. Alternatively, the group velocity can increase or even decrease with an increasing period.

1.3.2 Dispersion Curves

We have pointed out that the surface waves propagate along the surface of the Earth, with a ‘skin-depth’ that depends on the wavelength. Longer wavelengths penetrate deeper than shorter wavelengths and so, are more sensitive to the elastic properties of the deeper layers. On the contrary, short wavelengths ‘see’ the superficial layers.

Approximately, the depth up to which the medium is affected by the propagation of the wave is equal to a wavelength, and it is connected with the exponential decay of the particle motion. As a consequence, when considering the surface wave propagation in vertically heterogeneous media, it is expected that based on the frequency, they will involve different layers and so, the phase velocity will depend upon their mechanical properties. The surface wave velocity depends on the frequency, and this kind of plot is called dispersion curve 1.7 (a).

Phase and group velocity (for various periods) can be measured directly from the seismograms using different measurement techniques. One of the main interest in seismic tomography is to build an Earth model able to fit the observed surface wave dispersion. A common approach is to calculate theoretical dispersion curves for a given Earth model and compare them with the measured dispersion. A key point is to quantitatively understand which part of the Earth model (parameters as a function of depth) needs to be adjusted in order to fit the observed dispersion. For that, sensitivity kernels are calculated in order to map the relationship between phase and group velocities and the Earth structure. They determine the impact of changing the structure at a certain depth on the velocity of the waves 1.7 (b). Sensitivity kernels are equal to the partial derivatives of the Rayleigh phase and group velocity, usually with respect to the model parameters (like S-wave velocity, P-wave velocity, density) at different depths. The sensitivity of the surface wave velocities differs in amplitude and shape (as a function of parameter depths) for the various elastic parameters: for a fixed period, the sensitivity is maximum for S-wave speed and (usually) negligible for P-wave speed and density. This point will be better discussed in Chapters 4 and 5. The sensitivity kernels are used to invert the dispersion curves for shear-wave velocity profiles.

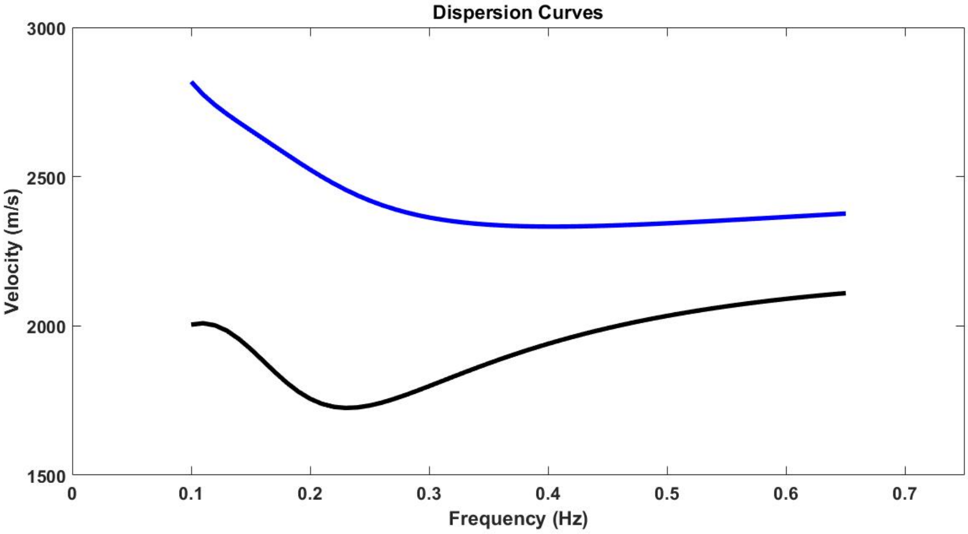

(a)

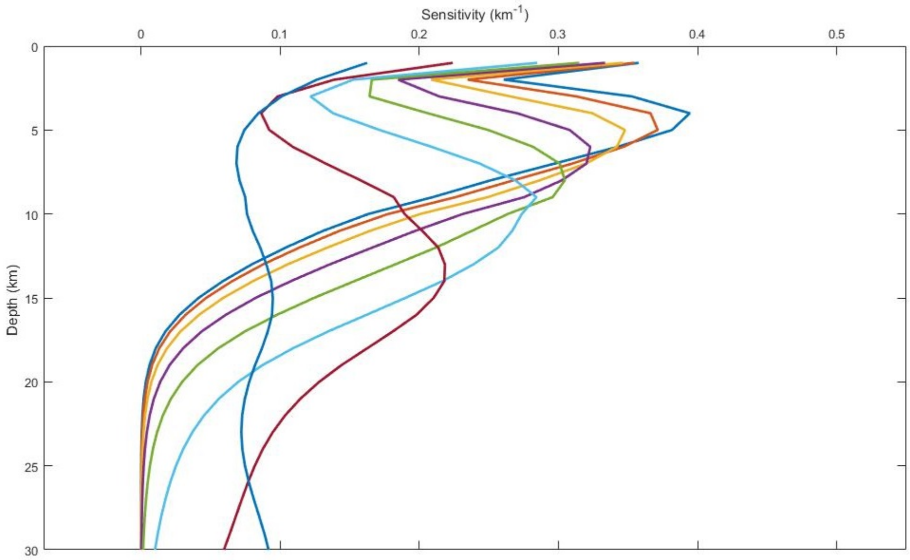

(b)

Figure 1.7: (a)Dispersion curves for phase (blue) and group (black velocity data. (b) Sensitivity kernel for phase velocity. The frequency range is $0.1 - 0.65$ Hz. Low-frequency kernels are peaked in deep depths, while high-frequency kernels in shallower depths.

Chapter 2

Forward Study for Rayleigh waves

Various methods of numerically calculating Rayleigh wave velocities for layered media can be found in the literature. A well-known method is the Thomson-Haskell Matrix Method [14], which seeks for the roots of the polynomial, formed by the calculation of the non-trivial solutions of the determinant of a square matrix, $|a(\omega, k)| = 0$, similar to the one presented in 1.2.2. According to the demonstration in 1.2.2, the roots are expected to be a function of the wavelength, k, and the angular frequency, ω.

Although, this way of handling the forward problem has been studied extensively by many scientists ([15],[14]) Haney and Tsai [1] suggest an other approach, which is based on Lysmer's work [6] and the *Thin Layer Method* by Kausel [16].

In this method, the forward problem turns out in a particular matrix formulation, as the layered medium is consistent horizontally and discrete vertically and so, it is represented by a finite-element system with given elastic properties. Then, the inversion approach, which is an extension of the finite-element method, is developed by perturbing the phase, or group, velocity in the material properties, which uses the same matrices used in the forward study.

In the next two sections of this chapter, I will introduce the fundamental theory behind the Thin Layer Method and some key points to take into consideration when the problem is treated numerically.

2.1 Lumped Mass Method for Rayleigh Waves

In this section, by following Lysmer [6], I show the process of calculating dispersion curves for Rayleigh waves.

Initially, the parametrization of the medium must be chosen. That means dividing the space into finite rectangular elements and assigning for each of them the appropriate elastic parameters, such as density ρ_j, shear modulus μ_j and the other Lamé coefficient $\lambda_j = \frac{2\mu_j \nu_j}{(1-2\nu_j)}$, noted the Poisson's ratio ν_j.

In order to study this system, some assumptions must be made:

1. The mass is considered to be at the element corners, thus the name lumped mass.

2. The displacement varies in the x and y direction according to

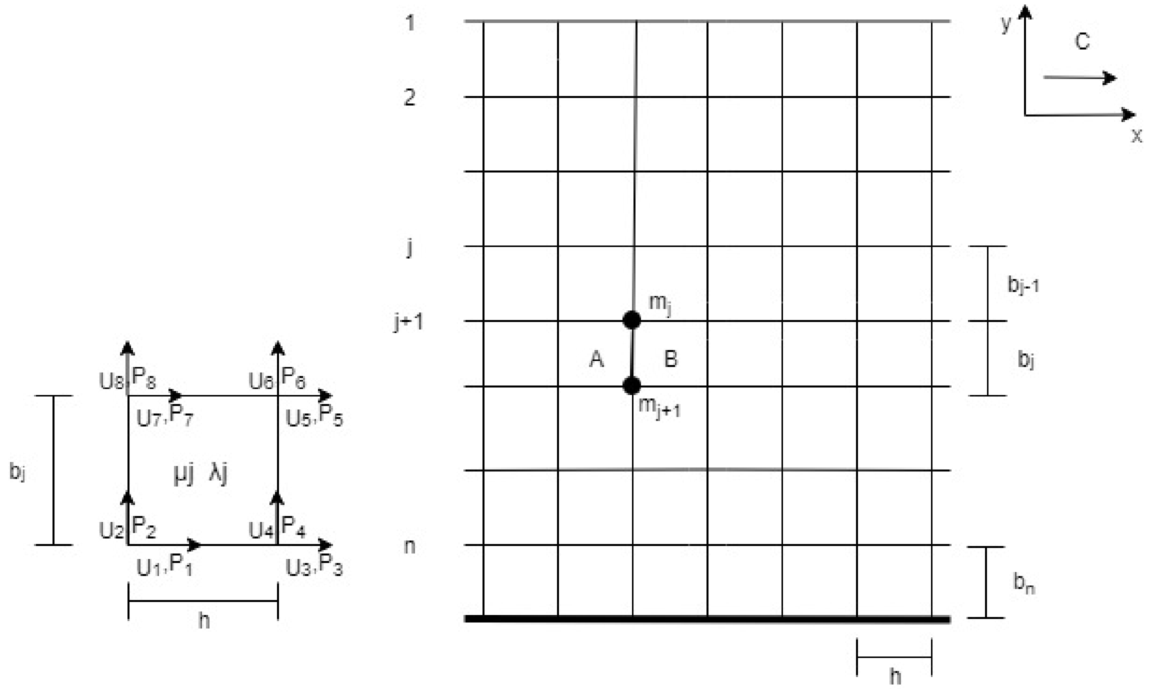

Figure 2.1: On the right: Representation of the layered system, and left: displacement and force field acting on corners between two elements

$$\begin{aligned} U_x &= c_1 x + c_2 y + c_3 xy + c_4 \\ U_y &= c_5 x + c_6 y + c_7 xy + c_8 \end{aligned} \tag{2.1}$$

with c_s $s = 1, ...8$ being arbitrary constants.

3. All forces are applied at the element corners.

The forces and the displacements can be represented by the vectors

$$\{U\} = \begin{Bmatrix} U_1 \\ U_2 \\ \vdots \\ U_8 \end{Bmatrix}, \{P\} = \begin{Bmatrix} P_1 \\ P_2 \\ \vdots \\ P_8 \end{Bmatrix} \tag{2.2}$$

and are connected by the linear relationship,

$$\{P\} = [K]_j \{U\} \tag{2.3}$$

due to the initial assumptions. The link between the two variables is an 8 × 8 symmetric matrix, that is called element stiffness matrix and whose elements are a function of the elastic constants. The matrix will not be presented in its initial formulation, but I will derive a 4 × 4 version of it during this demonstration.

For a plane harmonic wave propagating in the x-direction I can define,

$$\begin{aligned} U_x &= u_x(y)\exp i(\omega t - kx) \\ U_y &= iu_y(y)\exp i(\omega t - kx), \end{aligned} \tag{2.4}$$

with $c = \frac{\omega}{k}$ the phase velocity. For two adjacent elements A and B (figure 2.1 and 2.2), the displacement vectors are respectively,

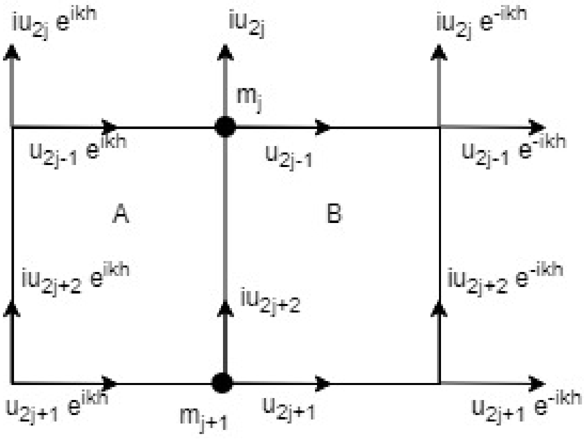
$iu_{2j}\,e^{ikh}$
iu_{2j}
$iu_{2j}\,e^{-ikh}$
m_j
$u_{2j-1}\,e^{ikh}$
u_{2j-1}
$u_{2j-1}\,e^{-ikh}$
A
B
$iu_{2j+2}\,e^{ikh}$
iu_{2j+2}
$iu_{2j+2}\,e^{-ikh}$
$u_{2j+1}\,e^{ikh}$
m_{j+1}
u_{2j+1}
$u_{2j+1}\,e^{-ikh}$

Figure 2.2: Displacements for the adjacent elements A and B

$$\{U\}_A = \begin{Bmatrix} u_{2j+1}\exp(ikh) \\ iu_{2j+2}\exp(ikh) \\ u_{2j+1} \\ iu_{2j+2} \\ u_{2j-1} \\ iu_{2j} \\ u_{2j-1}\exp(ikh) \\ iu_{2j}\exp(ikh) \end{Bmatrix} = [E]\{u\}_j \tag{2.5}$$

$$\{U\}_B = \{U\}_A \exp(-ikh) = \exp(-ikh)[E]\{u\}_j. \tag{2.6}$$

I have been also defined a simple matrix, $[E]$,

$$[E] = \begin{bmatrix} 0 & 0 & e^{ikh} & 0 \\ 0 & 0 & 0 & ie^{ikh} \\ 0 & 0 & 1 & 0 \\ 0 & 0 & 0 & i \\ 1 & 0 & 0 & 0 \\ 0 & i & 0 & 0 \\ e^{ikh} & 0 & 0 & 0 \\ 0 & ie^{ikh} & 0 & 0 \end{bmatrix} \tag{2.7}$$

and the so-called layer displacement vector, which corresponds to the displacement of the j-th layer,

$$\{u\}_j = \begin{Bmatrix} u_{2j-1} \\ u_{2j} \\ u_{2j+1} \\ u_{2j+2} \end{Bmatrix}. \tag{2.8}$$

Since the displacement vector is known, I expect to find the equivalent force vector for the two masses being at the corners of the sharing side of the elements A and B, namely m_j and m_{j+1}. This will happen by combining properly the expressions in 2.3 and 2.5 and again by consulting the figures 2.1 and 2.2. Consequently, I obtain

$$\begin{aligned} Q_{2j-1,j} &= \{K_5\}\{U\}_A + \{K_7\}\{U\}_B = (\{K_5\} + \{K_7\}\exp(-ikh))[E]\{u\}_j \\ iQ_{2j,j} &= \{K_6\}\{U\}_A + \{K_8\}\{U\}_B = (\{K_6\} + \{K_8\}\exp(-ikh))[E]\{u\}_j \\ Q_{2j+1,j} &= \{K_3\}\{U\}_A + \{K_1\}\{U\}_B = (\{K_3\} + \{K_1\}\exp(-ikh))[E]\{u\}_j \\ iQ_{2j+2,j} &= \{K_4\}\{U\}_A + \{K_2\}\{U\}_B = (\{K_4\} + \{K_2\}\exp(-ikh))[E]\{u\}_j \end{aligned} \tag{2.9}$$

where $\{K_r\}$ represents the r-th row of $[K]_j$.
Following the same path as in 2.8, the layer force vector is defined by

$$\{Q\}_j = \begin{Bmatrix} Q_{2j-1,j} \\ Q_{2j,j} \\ Q_{2j+1,j} \\ Q_{2j+2,j} \end{Bmatrix} \tag{2.10}$$

and so a similar to the 2.3 relation can be found for the 2.9,

$$\{Q\}_j = [L]_j\{u\}_j, \tag{2.11}$$

where $[L]_j$ (fig. 2.3) is a reduced layer stiffness matrix 4×4, real and symmetric, whose elements are in function of the same elastic properties as $[K]_j$.

In order to generalize for an n layer system, I shall write the displacement and force vector as,

$$\{u\} = \begin{Bmatrix} u_1 \\ u_2 \\ \vdots \\ u_{2n} \end{Bmatrix}, \{Q\} = \begin{Bmatrix} Q_1 \\ Q_2 \\ Q_3 \\ Q_4 \\ \vdots \\ Q_{2n-1} \\ Q_{2n} \end{Bmatrix} = \begin{Bmatrix} Q_{1,1} \\ Q_{2,1} \\ Q_{3,1} + Q_{3,2} \\ Q_{4,1} + Q_{4,2} \\ \vdots \\ Q_{2n-1,n-1} + Q_{2n-1,n} \\ Q_{2n,n-1} + Q_{2n,n} \end{Bmatrix} \tag{2.12}$$

Here as well, a relation of the form

$$\{Q\} = [K]\{u\} \tag{2.13}$$

can be defined by the relations 2.11 and 2.12. It is a $2n \times 2n$ matrix.
Newton's second law for the mass m_j is, for x and y direction respectively

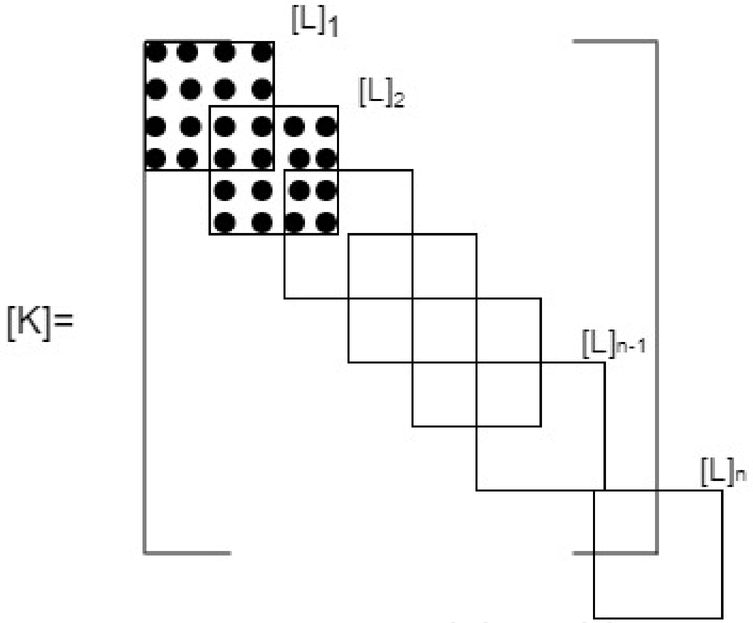

Figure 2.3: A schematic way to relate the matrix $[K]_j$ with $[L]_j$. The elemenents outside $[K]$ are not used.

$$\begin{aligned} -\omega^2 u_{2j-1} m_j &= -Q_{2j-1} \\ -i\omega^2 u_{2j} m_j &= -iQ_{2j}. \end{aligned} \tag{2.14}$$

Rewriting 2.14 in a generic form for the $2n$ equations of motion will give

$$\omega^2[M]\{u\} = \{Q\} \tag{2.15}$$

with $[M]$ being a $2n \times 2n$ diagonal mass matrix, with terms

$$\begin{bmatrix} m_{2j-1,2j-1} & \\ & m_{2j,2j} \end{bmatrix} = m_j,\ j = 1, \ldots, n. \tag{2.16}$$

At this point, a clear link exists between 2.13 and 2.15, and so I will substitute the first expression to the second expression and obtain the following eigenvalue problem in terms of the unknown displacements $\{u\}$

$$([K] - \omega^2[M])\{u\} = \{0\} \tag{2.17}$$

A further simplification may occur in case of introducing the vector $\{\nu\}$, defined by $\{u\} = [M]^{\frac{-1}{2}}\{\nu\}$,

$$([B] - \omega^2[I])\{\nu\} = \{0\}, \tag{2.18}$$

with $[B] = [B(k)]$, a real symmetric matrix with elements $b_{ij} = k_{ij}/\sqrt{m_i m_j}$.

I expect $2n$ real positive eigenvalues ω_i^2, and the associated $\{\nu\}_i$ eigenvectors to form the solution of the 2.18.

Summarizing, Lysmer [6] proposes that for a given value of the wave number k and with the appropriate choice of the matrix $[K]$, which is properly modified to the matrix $[B]$, the eigenvalue problem in 2.18 is solved and for each mode, the frequency ω_i and thus, the phase velocity c_i can be found. Every pair of (ω_i, c_i) forms the $2n$ dispersion curves.

2.2 Forward numerical modeling

Although the forward solver of Haney and Tsai [1] used in the present work is primarily based on Lysmer's [6] approach discussed in 2.1, there are some key differences worth noting.

The Rayleigh-wave eigenfunction is represented by a system of N linear finite elements and the corresponding physical properties by boxcar functions, similar to the figure 2.4.

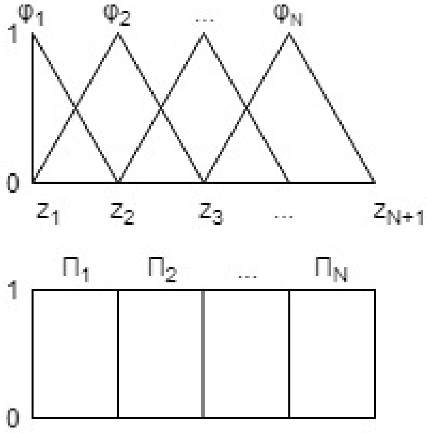

Figure 2.4: Displacements for the adjacent elements A and B

While there are N elements in the grid, exists $N+1$ nodes: that is chosen to be in accordance with Nolet's locked mode approximation [17], which treats the last layer as a perfect reflector, meaning that there is no response coming from the rigid bottom.

A similar to 2.18 eigenvalue problem can be found, if

$$\mathbf{v} = [\ldots r_1^{K-1},\ r_2^{K-1},\ r_1^K,\ r_2^K,\ r_1^{K+1},\ r_2^{K+1} \ldots]^T \tag{2.19}$$

with K representing the number of element and r_1 and r_2 being the eigenfunctions representing the horizontal and vertical nodal displacements respectively, and so

$$(k^2\mathbf{B}_2 + k\mathbf{B}_1 + \mathbf{B}_0)\mathbf{v} = \omega^2\mathbf{M}\mathbf{v}. \tag{2.20}$$

In the 2.20, the $\mathbf{B}_0$, $\mathbf{B}_1$, $\mathbf{B}_2$ represent the stiffness matrices, which are real and symmetric and similarly to Lysmer [6] depend on the elastic properties ρ, λ and μ but are developed as Kausel [16]. The way to calculate them is presented in Appendix A.

As claimed by Haney and Tsai [1], instead of solving in terms of the angular frequency for a known wavenumber, usually a more reasonable treatment of the problem would be solving in terms of the wavenumber.

This leads in reformulating the problem as

$$k\mathbf{B}_2\mathbf{a} = \omega^2\mathbf{M}\mathbf{v} - \mathbf{B}_1\mathbf{a} - \mathbf{B}_0\mathbf{v} \tag{2.21}$$

where $\mathbf{a} = k\mathbf{v}$, a variable which facilitates the calculation.

So, the generalized linear eigenvalue problem to be solved is

$$k\begin{bmatrix}\mathbf{I} & 0\\ 0 & \mathbf{B}_2\end{bmatrix}\begin{bmatrix}\mathbf{v}\\ \mathbf{a}\end{bmatrix} = \begin{bmatrix}0 & \mathbf{I}\\ \omega^2\mathbf{M} - \mathbf{B}_0 & -\mathbf{B}_1\end{bmatrix}\begin{bmatrix}\mathbf{v}\\ \mathbf{a}\end{bmatrix}. \tag{2.22}$$

As soon as the above calculation is done for a given mode, the group velocity may also be computed by perturbing both wavenumber k and frequency ω, while the stiffness matrices should stay as they are. Hence, the formula is

$$U = \frac{\delta\omega}{\delta k} = \frac{\mathbf{v}^T(2k\mathbf{B}_2 + \mathbf{B}_1)\mathbf{v}}{2\omega\mathbf{v}^T\mathbf{M}\mathbf{v}}. \tag{2.23}$$

Some further key elements regarding the forward modeling to be made are the accuracy and whether a mode is guided or not for a given frequency in a certain depth.

The accuracy problem is bounded to the sensitivity depth of Rayleigh waves. Haney and Tsai [1] have noticed that for a specific mode the sensitivity depth can be found by $0.5m\lambda$, where $m = 1, 2, \dots$ represents the fundamental mode, first overtone etc. Numerically, this can be controlled by appropriately defining the total depth of the model and the thickness of the elements.

The depth of the model must be large enough in order to satisfy the already mentioned locked-mode approximation, which is equivalent to the "vanishing condition at infinite depth". This demands the total depth, H, to be greater than the maximum wavelength, which may also correspond to the maximum sensitivity depth,

$$H > m\lambda,\ (H > 2z_{max}). \tag{2.24}$$

Regarding the thickness of the elements, h_N, the wavelength must be larger (in the present work five times) than the elements' thickness in order to sample properly at each depth,

$$\lambda > 5h_N. \tag{2.25}$$

For the exclusion of the non-guided modes, the vertical component of the nodal displacements is compared to a linear function decreasing from the surface to the bottom of the model. More precisely, the model is divided in two halfs: then, for the linear function, the ratio of the depth integral for the first half (0 to $H/2$) to the depth integral for the second half ($H/2$ to H) is required to be equal to three. If the equivalent ratio for an eigenvector is less than three, which means that is not decaying fast enough, then it is considered as non-guided.

Chapter 3

Inverse Problem Theory

In Chapter 2, I have seen how to deal with the forward problem: from the shear-wave velocity structure to the Rayleigh-wave dispersion curves. So, if Earth's structure is assumed known and by using the propagation theory, the data can be predicted.

The inverse problem, as its name suggests, is working *backwards*. From the data, which, in my case, are the observed Rayleigh-wave phase velocities as a function of period (dispersion curves), I need to find the realistic velocity structure that predicts the data. This problem is commonly faced by solving the inverse problem which can be formulated with different approaches. For instance, in this work two different inversion methods are used: the perturbational method for the iterative improvement of an initial model, and the nonperturbational method which might provide a good initial model (to be further improved by the perturbational method).

In the next two sections, I will give the basic theory of the Inverse Problem, following the statistical approach defined by the Bayesian framework introduced by Tarantola [18], together with the perturbational approach, by Haney and Tsai [1], used at the data analysis part of this thesis. The last section is about the nonperturbational method, which originates from the Dix formula [1].

3.1 Bayesian formulation for inverse problems

Solving an inverse problem means to seek for a solution of the following system,

$$\mathbf{d} = g(\mathbf{m}) \tag{3.1}$$

where **d** are the data, **m** the model parameters to be found and g the forward operator.

In order to do that, I first have to solve the forward problem, in which by starting from an estimated model, we *predict* what the observations should be.

The solution of the inverse problem comes from the minimization of the misfit of a functional which represents the differences between the observations and the predictions. This is a deterministic point of view.

Since, in general the predicted values are different from the observed ones due to uncertainties in measurements and modelization, the best way to describe any *state of information* is by probability densities.

For this reason, a probabilistic form of the 3.1 is needed [18], which will connect the physical theory, the information on the model and the measurements (data).

The theoretical state of information can be represented by the joint probability density $\Theta(\mathbf{d}, \mathbf{m})$ which provides the existent correlations in the physical theory. As for every joint probability density can be expressed by the product of a marginal and a conditional, I can write,

$$\Theta(\mathbf{d}, \mathbf{m}) = \theta(\mathbf{d}|\mathbf{m})\mu_M(\mathbf{m}) \tag{3.2}$$

where $\mu_M(\mathbf{m})$ is the homogeneous probability density as marginal for the model parameters and $\theta(\mathbf{d}|\mathbf{m})$ the probability density of d given $\mathbf{m}$.

At this point, one can assume different types of probabilistic model to express the conditional probability density in the 3.2. If Gaussian uncertainties with covariance matrix $\mathbf{C_T}$ are assumed then we obtain,

$$\Theta(\mathbf{d}, \mathbf{m}) = const \exp{(-\frac{1}{2}(\mathbf{d} - \mathbf{g}(\mathbf{m}))^T\mathbf{C_T^{-1}}(\mathbf{d} - \mathbf{g}(\mathbf{m})))}\mu_M(\mathbf{m}). \tag{3.3}$$

Regarding the measurements, which depend on uncertainties, in order to find the corresponding state of information, I first must know the statistics of the instrument from which the measurements are obtained. Let us assume that for an input $\mathbf{d}$ of the instrument, its output is $\mathbf{d_{out}}$. I then can define the conditional probability density, $\nu(\mathbf{d_{out}}|\mathbf{d})$, for the $\mathbf{d_{out}}$ values given $\mathbf{d}$.

If I assume a linear data space (which means that $\mu_D(\mathbf{d})$ is constant), the joint probability density can be written

$$f(\mathbf{d_{out}}, \mathbf{d}) = \mu_D(\mathbf{d})\nu(\mathbf{d_{out}}|\mathbf{d}). \tag{3.4}$$

Also, if $\mathbf{d_{out}} = \mathbf{d_{obs}}$, then the conditional probability density to obtain $\mathbf{d}$ when the observed values are $\mathbf{d_{obs}}$ is

$$\rho_D(\mathbf{d}) = f(\mathbf{d}|\mathbf{d_{obs}}) = \frac{\mu_D(\mathbf{d})\nu(\mathbf{d_{obs}}|\mathbf{d})}{\int_D d\mathbf{d}\mu_D(\mathbf{d})\nu(\mathbf{d_{obs}}|\mathbf{d})} \tag{3.5}$$

Again, I assume Gaussian uncertainties with C_D the covariance matrix and obtain,

$$\rho_D(\mathbf{d}) = const \exp{(-\frac{1}{2}(\mathbf{d} - \mathbf{d_{obs}})^T C_D^{-1}(\mathbf{d} - \mathbf{d_{obs}}))}. \tag{3.6}$$

The prior information of the model parameters, has no connection to the data. If there is no kind of a priori information then,

$$\rho_M(\mathbf{m}) = \mu_M(\mathbf{m}) \tag{3.7}$$

where $\mu_M(\mathbf{m})$ is the model parameters' homogeneous probability density.

On the other hand, if it is of Gaussian type I obtain,

$$\rho_M(\mathbf{m}) = const \exp{(-\frac{1}{2}(\mathbf{m} - \mathbf{m}_{prior})^T C_M^{-1}(\mathbf{m} - \mathbf{m}_{prior}))}, \tag{3.8}$$

where $\mathbf{m}_{prior}$ is mean of the distribution and C_M the covariance matrix.

Let's consider the probability density $\rho(\mathbf{d}, \mathbf{m})$, which express the information that I have on model $\mathbf{m}$ and observable $\mathbf{d}$ parameters. This constitutes the a priori information, which in combination with the probability density of the physical theory $\Theta(\mathbf{d}, \mathbf{m})$, can give the a posteriori state of information described by the probability density $\sigma(\mathbf{d}, \mathbf{m})$. In other words, the *conjuction* of the two states of information have produced,

$$\sigma(\mathbf{d}, \mathbf{m}) = k \frac{\rho(\mathbf{d}, \mathbf{m})\Theta(\mathbf{d}, \mathbf{m})}{\mu(\mathbf{d}, \mathbf{m})} \tag{3.9}$$

where $\mu(\mathbf{d}, \mathbf{m}) = \mu_D(\mathbf{d})\mu_M(\mathbf{m})$ and k a normalization constant.

Fron the equation 3.9, I can find the posterior information on the model parameters $\mathbf{m}$, through the marginal probability density,

$$\sigma_M(\mathbf{m}) = \int_D d\mathbf{d}\sigma(\mathbf{d}, \mathbf{m}). \tag{3.10}$$

As mentioned above, the information for the data has been obtained independently of the information of the model parameters and thus, I can write

$$\rho(\mathbf{d}, \mathbf{m}) = \rho_D(\mathbf{d})\rho_M(\mathbf{m}) \tag{3.11}$$

This, together with the equations 3.2 and the $\mu(\mathbf{d}, \mathbf{m}) = \mu_D(\mathbf{d})\mu_M(\mathbf{m})$ can reduce the model posterior information in

$$\begin{aligned} \sigma_M(\mathbf{m}) &= k\rho_M(\mathbf{m}) \int_D d\mathbf{d} \frac{\rho_D(\mathbf{d})\theta(\mathbf{d}|\mathbf{m})}{\mu_D(\mathbf{d})} \\ &= k\rho_M(\mathbf{m})L(\mathbf{m}) \end{aligned} \tag{3.12}$$

where $L(\mathbf{m})$ is the so-called likelihood function, which describes how well a model $\mathbf{m}$ is in interpreting the data $\mathbf{d}$.

In order to proceed, one must know whether the forward problem is linear or not.

In the first case, where $\mathbf{d} = \mathbf{G}\mathbf{m}$, and if the equations 3.3, 3.6 and 3.8 are still valid, I expect to obtain a Gaussian posterior probability density as well. The solution will be the one m_s that minimizes the misfit function,

$$2S(\mathbf{m}) = \|\mathbf{G}\mathbf{m} - \mathbf{d}_{obs}\|_D^2 + \|\mathbf{m} - \mathbf{m}_{prior}\|_M^2 \tag{3.13}$$

meaning that $\mathbf{m_s}$ and $\mathbf{Gm_s}$ are close to $\mathbf{m}_{prior}$ and $\mathbf{d}_{obs}$ respectively.

For a nonlinear problem, $\mathbf{d} = \mathbf{g}(\mathbf{m})$, $\sigma_M(\mathbf{m})$ is not Gaussian.

For certain problems though, the forward equation can be linearised around $\mathbf{m}_{prior}$ and then $\sigma_M(\mathbf{m})$ will be approximately Gaussian, and the solution will be equivalent to the one of the linear problem.

In case of non-linearity, iterative algorithms are preferred. They converge to an optimal point after some iterations. An example of this case is the inversion of surface wave dispersion curves.

3.2 Perturbational Inversion

The perturbational inversion approach that is used in the present work is proposed by Haney and Tsai [1] and is based on the perturbation of the material properties and wavenumber while maintaining fixed the frequency [15]. This is how the perturbations in phase velocity are calculated and given by,

$$\begin{aligned}\frac{\delta c}{c} = \frac{1}{2k^2 U c \mathbf{v}^T \mathbf{M} \mathbf{v}} \Big(\sum_{i=1}^{N} \frac{\partial (k^2 \mathbf{B}_2 + k \mathbf{B}_1 + \mathbf{B}_0)}{\partial \mu_i} \mathbf{v} \delta \mu_i \\ + \sum_{i=1}^{N} \mathbf{v}^T \frac{\partial (k^2 \mathbf{B}_2 + k \mathbf{B}_1 + \mathbf{B}_0)}{\partial \lambda_i} \mathbf{v} \delta \lambda_i - \omega^2 \sum_{i=1}^{N} \mathbf{v}^T \frac{\partial \mathbf{M}}{\partial \rho_i} \mathbf{v} \delta \rho_i \Big) \qquad (3.14)\end{aligned}$$

The formula 3.14 indicates how a perturbation in the model parameters affects the phase velocity. Basically, the inverse problem is solved together with the forward problem: first, the predicted phase velocity data are calculated from an initial model, and then the appropriate model perturbations are found, which will bring the predicted phase-velocity dispersion curve close to the observed one (real data). The model perturbation, which after a number of iterations will fit accurately the observations/data, is the resulting model from the whole inversion process.

The equation 3.14 applies to the mode of interest.

The stiffness matrices used in Chapter 2 for solving the forward problem are exactly the same with those in equation 3.14. This great advantage is presented clearly by using the matrix-vector notation.

By calculating the 3.14 for many frequencies and after defining the phase velocity kernels for μ, λ and ρ, the above equation takes the form of

$$\frac{\delta \mathbf{c}}{\mathbf{c}} = \mathbf{K}_{\mu}^{\mathbf{c}} \frac{\delta \mu}{\mu} + \mathbf{K}_{\lambda}^{\mathbf{c}} \frac{\delta \lambda}{\lambda} + \mathbf{K}_{\rho}^{\mathbf{c}} \frac{\delta \rho}{\rho}. \qquad (3.15)$$

Although, this is a linear relation between the perturbations in c and the three material properties perturbations, I prefer to invert for shear wave velocity profiles, because the change in shear-wave velocity produce great changes in Rayleigh-wave velocity [5]. So, an equivalent perturbational relation between Rayleigh phase (or group) and shear wave velocity is found.

The authors developed two ways to invert: the first one is to maintain fixed the Poisson's ratio and the density and the second one the P-wave velocity and density.

In the first case, I can use the following equations that describe the relative perturbation in shear modulus and Lamé's coefficient,

$$\begin{aligned}\frac{\delta \lambda}{\lambda} &= \Big(\frac{2\alpha^2}{\alpha^2 - 2\beta^2}\Big)\frac{\delta \alpha}{\alpha} - \Big(\frac{4\beta^2}{\alpha^2 - 2\beta^2}\Big)\frac{\delta \beta}{\beta} + \frac{\delta \rho}{\rho} \\ \frac{\delta \mu}{\mu} &= 2\frac{\delta \beta}{\beta} + \frac{\delta \rho}{\rho}.\end{aligned} \qquad (3.16)$$

For the Poisson's ratio to be constant means that the P-wave to S-wave velocity ratio will be constant as well ($\alpha/\beta = R$) together with their relative perturbations ($\delta\alpha/\alpha = \delta\beta/\beta$).

So, substituting in 3.15 we obtain,

$$\frac{\delta \mathbf{c}}{\mathbf{c}} = \mathbf{2}(\mathbf{K}^{\mathbf{c}}_{\mu} + \mathbf{K}^{\mathbf{c}}_{\lambda})\frac{\delta\beta}{\beta} = \mathbf{K}^{\mathbf{c},\mathbf{R}}_{\beta}\frac{\delta\beta}{\beta}. \tag{3.17}$$

The kernel $K^{c,R}_{\beta}$ of the shear wave velocity is defined as twice the sum of the λ and μ material kernels.

Again, the relations in 3.16 will be used, in order to proceed for the second case, but first I will express them in matrix-vector notation,

$$\begin{aligned} \frac{\delta\lambda}{\lambda} &= \mathbf{D_1}\frac{\delta\alpha}{\alpha} - \mathbf{D_2}\frac{\delta\beta}{\beta} + \frac{\delta\rho}{\rho} \\ \frac{\delta\mu}{\mu} &= \mathbf{2}\frac{\delta\beta}{\beta} + \frac{\delta\rho}{\rho} \end{aligned} \tag{3.18}$$

where D_1 and D_2 are matrices with entries in the main diagonal defined by the initial relation.

Applying in the 3.18 for the two defining conditions gives,

$$\frac{\delta \mathbf{c}}{\mathbf{c}} = (\mathbf{2}\mathbf{K}^{\mathbf{c}}_{\mu} - \mathbf{K}^{\mathbf{c}}_{\lambda}\mathbf{D_2})\frac{\delta\beta}{\beta} = \mathbf{K}^{\mathbf{c},\alpha}_{\beta}\frac{\delta\beta}{\beta}. \tag{3.19}$$

In contrast to the first case, this result is a weighted sum of the involved kernels.

Needless to say that both resulting relations 3.17 and 3.19 are for perturbations in phase velocity. Similar to these two relations can be obtained for group velocities too [19],

$$\mathbf{K}^{U}_{\beta} = \mathbf{K}^{c}_{\beta} + \frac{U\omega}{c}\frac{\partial \mathbf{K}^{c}_{\beta}}{\partial\omega} \tag{3.20}$$

$$\frac{\delta \mathbf{U}}{\mathbf{U}} = \mathbf{K}^{U}_{\beta}\frac{\delta\beta}{\beta}. \tag{3.21}$$

In the codes the absolute perturbations are used and so the perturbation kernels can be written as,

$$\mathbf{G}^{c}_{\beta} = diag(\mathbf{c})\mathbf{K}^{c}_{\beta}diag(\beta)^{-1}. \tag{3.22}$$

Solving this kind of inverse problem needs a sort of regularization in order to obtain smooth and stable solutions. That means that both data and model must be weighted properly. A good approach is the weighted-damped least square method [1], with which the calculation is made by two weighted matrices, one for the model and one for the data (equation 3.24). A good choice for these weighted matrices is the inverse of the equivalent covariance matrices 3.23. This implies that, data with large variance are weighted less (not so accurate) than data with small variance (more accurate) while for the model provides a way to control the *distance* from the a priori model parameters.

---

[1] Weighted-damped least square method can be thought of as a weighted combination of weighted minimum length solutions and weighted least squares [20], [21]

Data and model covariance are given by

$$\begin{aligned}\mathbf{C}_d(i,i) &= \sigma_d(i)^2 \\ \mathbf{C}_m(i,j) &= \sigma_m^2 \exp\left(-\left|z_i - z_j\right|/d\right)\end{aligned} \tag{3.23}$$

where $\sigma_d(i)$ and σ_m is the data standard deviation and model standard deviation respectively, $z_i - z_j$ describes the distance between the i-th and j-th elements, and d is the correlation length, which is chosen with respect to the desired extend of smoothing. I will discuss more the choice of this parameter at the second part of this thesis. The $\mathbf{C}_d$ is diagonal, which means that the data errors are uncorrelated. The model standard deviation is calculated by multiplying a user-supplied factor with the mean of the data standard deviation over all frequencies.

The algorithm of total inversion [7] is used to calculate the model updates β_n,

$$\begin{bmatrix}\mathbf{C}_d^{-1/2} \\ 0\end{bmatrix}\left(\mathbf{U}_0 - \mathbf{f}(\beta_{n-1}) + \mathbf{G}_\beta(\beta_{n-1} - \beta_0)\right) = \begin{bmatrix}\mathbf{C}_d^{-1/2}\mathbf{G}_\beta \\ \mathbf{C}_m^{-1/2}\end{bmatrix}(\beta_n - \beta_0). \tag{3.24}$$

The forward operator is f and the data are the U_0. In this equation the top row represents the data equation, while the bottom row the model equation: I note that they appear symmetrically in the 3.24.

This damped inversion starts from an initial model and consecutively, calculates its updates: at every iteration the dispersion curves and the partial derivatives are computed in order to calculate the data discrepancy for the current update and modify the model parameters accordingly. The total number of updates depends upon the value of the chosen stopping criterion ,

$$\chi^2 = (\mathbf{f}(\beta_n) - \mathbf{U_0})^T \mathbf{C}_d^{-1}(\mathbf{f}(\beta_n) - \mathbf{U}_0)/F \tag{3.25}$$

which is the *reduced* χ^2 with F being the number of measurements used. The iterative process will stop at the n-th update model, which means that the current χ^2 value is less than a certain value, chosen by the user.

3.3 Nonperturbational inversion

The inversion method described in the previous section, improves efficiently any initial model. However, not in all the Earth regions exist acceptable initial models. Haney and Tsai [10] have extended the Dix equation, well-known in reflection seismology for the determination of the velocities in the layered subsurface, in order to construct shear-wave velocity profiles from phase or group velocity data. These 1D profiles can then be used as initial models for nonlinear inversion.

If I consider a sequence of flat and parallel layers and all the potential reflections made from it, the Dix equation provides the interval velocity of the n-th layer based on the stacking velocities and the reflection arrival times. This is derived when solving the equation 3.26 with the assumption of short offsets,

$$V_{st,n} = \sqrt{\frac{\sum_{i=1}^{n} V_i^2 \Delta t_i}{\sum_{i=1}^{n} \Delta t_i}}, \tag{3.26}$$

where $V_{st,n}$ is the stacking velocity of the n-th interface, V_i is the velocity and Δt_i is the vertical two-way travel time through the i-th layer, which is a kind of weighting.

The equation 3.26 can be extended to the surface waves by considering the phase or group velocity as the stacking velocity and the shear-wave velocity as the interval velocity for each layer (3.26). The weighting factor is a kernel, which is based on the associated eigenfunctions of Rayleigh-waves. The counterpart of 3.26 in the surfaces waves is,

$$\mathbf{c}^2 = \mathbf{G}\beta^2. \tag{3.27}$$

It is straightforward to observe that the equation 3.27 is a direct and not some kind of perturbative relation between the phase and the shear-wave velocity, in contrast of the equations 3.17 and 3.19.

This inversion method is based on weighted-damped least squares, as it is in the perturbative one. The covariance matrices for both model and data, are calculated in the same manner. However, in this nonperturbative inversion code, in order to best choose the correlation length and the model standard deviation factor (3.23), an appropriate range for both parameters needs to be defined over which the inversion problem is solved. The initial model is the average of all models, resulting from the nonperturbational inversion, that fall into the acceptable χ^2 window, supplied by the user.

The linear inversion scheme is given by

$$\begin{bmatrix} \mathbf{C}_d^{-1/2}\mathbf{G} \\ \mathbf{C}_m^{-1/2} \end{bmatrix} \beta^2 = \begin{bmatrix} \mathbf{C}_d^{-1/2}\mathbf{c}^2 \\ \mathbf{C}_m^{-1/2}\beta_0^2 \end{bmatrix}, \tag{3.28}$$

where β_0 is the shear-wave velocity obtained on the basis of the mapping of the data at the minimum and maximum sensitivity depth ([5]). This kind of mapping generates the model in this depth range. In order to extend the model in areas of poor resolution linear extrapolation is made, i.e above and below the resolution depths. By using the Dix-type method the final update will be an update of such kind data-driven model.

For fundamental mode phase velocity measurements, there are three ways to proceed with the linear inversion. The simple case is to assume that a Rayleigh wave is propagating, at each frequency, in a different homogeneous medium, with any value of Poisson's ratio. The other two cases, which are more accurate, are based on the assumption that the shear-wave velocity profile is described by power laws, with Poisson's ratio of 0.25 and 0.3.

Part II

Data Analysis

Chapter 4

Synthetic Testing

4.1 A short description of the Software Tools

The theory explained in the previous chapters is implemented in a set of MATLAB codes, that I modified to better achieve the purpose of this thesis. The software, namely the RAYLEE package, for the inversion of both synthetic and real data, was downloaded from the Society of Exploration Geophysicists (SEG) site [22]. The codes can be used in order to generate Rayleigh wave phase or group velocities (in case of synthetic tests), define the desired initial model and invert for shear-wave velocity profiles in crustal and near-surface scale. Inversions in crustal scale can be made for both continental and oceanic crust, by adding a water layer on top of the model. It is also capable of joint inversions of the fundamental and higher modes.

4.1.1 Optimal Layering

When dealing with inversion of surface-wave dispersion curves using finite-element based methods, attention must be paid to the layering of the model for the numerical calculation. An array of elements with equal thickness is simple but not efficient as a choice of layering: the waves need to be properly sampled at each depth, otherwise they tend to be oversampled in depth for properly sampling at surface, which might lead to instability problems and longer runtimes for the algorithm, and undersampled in surface for properly sampling in depth, which will generate a not so representative smooth model for the superficial layers. So, in order to prevent from wrong sampling of the waves, a computational grid with increasing element thickness in depth appears to be a more reasonable choice.

As a rule of thumb, a Rayleigh-wave phase velocity c with a wavelength l can mostly be related to shear-wave velocity at an indicative depth equal to

$$z = al \tag{4.1}$$

where a can take the values 0.63 ([5]) or 0.5 ([10]). This depth is the sensitivity depth of Rayleigh waves. So, for a given dispersion curve, I am able to find the minimum and maximum wavelength (l_{min}, l_{max}) and by extension the depth range where the sensitivity is maximum.

Consequently, on the basis of the above considerations about z_{min} and z_{max} can be defined an optimal layering for Rayleigh-wave modelling.

First, I will see how to calculate the thickness of the layers lying in (z_{min}, z_{max}) and then for the rest of them in $(0, z_{min})$ and (z_{max}, ∞).

Let's define a layer density as a function of wavelength given by,

$$\rho_{layers}(l) = n/l \tag{4.2}$$

where n is the desired number of layers to be sampled per wavelength. In terms of the sensitivity depth, the relation 4.2 can be expressed by

$$\rho_{layers}(z) = na/z. \tag{4.3}$$

By integrating the relation 4.3 for the domain (z_{min}, z), which lies inside (z_{min}, z_{max}), the equivalent number of layers up to that depth, z, can be found,

$$\int_{z_{min}}^{z} \rho_{layers}(z')dz' = N(z). \tag{4.4}$$

The integration 4.4 gives,

$$N(z) = na \ln\left(\frac{z}{z_{min}}\right). \tag{4.5}$$

In the same path, if the integration domain is the (z_{min}, z_{max}), then the maximum number of layers, N_{max}, can be found.

If I express the 4.5 relation, in terms of the depth of the layer interfaces I get,

$$z(N) = z_{min} \exp\left(\frac{N}{na}\right), \tag{4.6}$$

and its derivative with respect to the number of layers N, calculates approximately the thickness of the N-th layer.

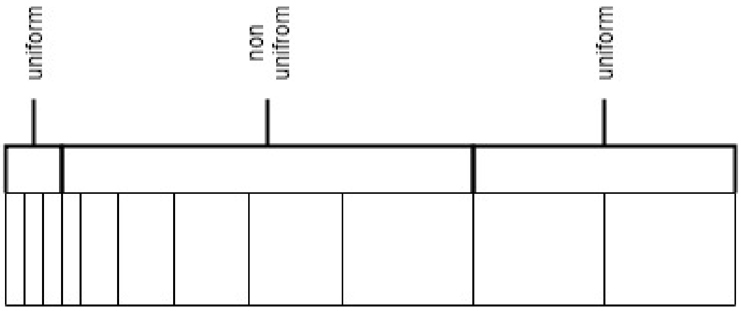

Figure 4.1: The optimal grid vector

The thicknesses increase exponentially from the first layer, whose interface is at z_{min}, up to the last layer at z_{max} depth. This is how I obtain an optimal nonuniform layering for the Rayleigh waves.

The relation 4.1 implies that Rayleigh waves are not sensitive to the domains $(0, z_{min})$ and (z_{max}, ∞), but this is not rigorous since this relation is an approximate one. I impose uniform grids for both domains: the thicknesses in $(0, z_{min})$ are equal to the first, and also minimum, layer thickness in (z_{min}, z_{max}), while the thicknesses in (z_{max}, ∞) are equal to the last, and so maximum, thickness layer in (z_{min}, z_{max}) as well. The complete layering is presented in the figure 4.1.

4.1.2 Smoothness Scale

The smoothness scale, or correlation length, as mentioned above, is the parameter d on the denominator of the exponential function in the relation 3.23. It smooths out the spatial variations in the model space and contributes to how the inversion updates the size of heterogeneities. It depends on the surface waves' wavelength.

In the finite-element approach and on the basis of the extension of the desired spatial smoothness, usually it is a fixed value and equal to a multiple of the element thickness. For instance, Haney and Tsai [1] posed it equal to four times the element thickness while, Gerstoft et al. [23] twice, in their applications. In both cases the grid was uniform.

It appears appropriate to use a smoothness scale that will not be fixed, but will be variable with depth and still dependent on the element thickness. For the nonuniform grid, and since the element thickness increase with depth, the smoothness scale will increase too and will be equal to the sum of the thickness of two adjacent elements.

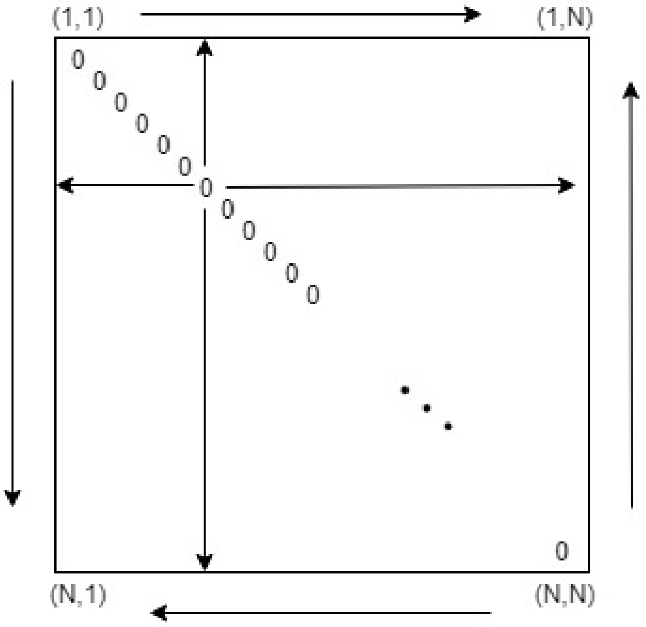

Figure 4.2: The $N \times N \left|r_i - r_j\right|$ matrix; the zeros in the diagonal correspond to the each one of the N elements (layers).The arrows indicate the direction of the increasing depth (the use of the word *depth*, in the present context does not necessarily imply that the direction of the measurment is from the surface to the bottom).

Let us consider an N element grid vector. Then, the numerator of the fraction in the model covariance matrix 3.23, will be an $N \times N$ matrix, whose diagonal entries (i, i) are zeros and represent the top of the i-th element. Every previous or subsequent elements of the (i, i), either in column or row, represents the distance between the top of the i-th and that element, which is equal to the in-between grid spacing (figure 4.2). Consequently, and with respect to the diagonal of the $N \times N$ matrix, the depth increases by starting

1. from the surface and moving towards the bottom, passing from the element $(1,1)$ to the elements $(1,N)$ and $(N,1)$ and,
2. from the bottom and moving towards the surface, passing from the element (N,N) to the elements $(1,N)$ and $(N,1)$

Taking this into consideration, and after creating a vector of N elements by summing the thickness of every two adjacent elements of the grid vector, the smoothness scale $N \times N$ matrix can be created by placing the aforementioned vector in the same direction/manner as the depth increases in the $\left|z_i - z_j\right|$ matrix.

In this chapter, the smoothness scale is chosen to be fixed. In next chapter, where some cases of real data are tested, the matrix smoothness has been used.

4.2 Analysis of the earth model parameters impact on dispersion curves

Rayleigh-wave velocity is strongly depended on four parameters: the shear-wave velocity Vs, the longitudinal wave velocity Vp, the density ρ and the thickness of the layers. Every parameter has a different impact on the phase velocity dispersion curve for a certain frequency range and in order to confirm and evaluate it, in the present section, I present the parameters' profiles together with the equivalent dispersion curves, after varying, in the same manner, one parameter at a time. That is to say, the forward problem is solved twice, first for the initial model and second, for a variation of its own. This test is of high importance as it determines which one of the parameters is more indicated to be inverted. If the effects on dispersion curve are considered small for a certain parameter, then this parameter may not be appropriate to invert for. A similar testing method has being used by Molinari [24] to study the impact of the parameters on dispersion of surface waves.

Three variations have been applied on the profile of every parameter and that is, an increase of 2.5% of the value of the parameter in the following domains

1. $0 - 24$ km (panels (a) and (b) in figures 4.3, 4.4, 4.5),
2. $24 - 150$ km (panels (c) and (d) in figures 4.3, 4.4, 4.5),
3. $150 - 400$ km (panels (e) and (f) in figures 4.3, 4.4, 4.5).

The initial model used for this test is the same as the one used for testing the real data in section 5.2, for the case of Northern Alpine foreland. The frequency range is $(0.02 - 0.2)$ Hz.

Since the total thickness of the model is equal to 400 km, it appears reasonable to link the first domain $(0 - 24km)$ to the crustal part and the other two, $(24 - 150km)$ and $(150 - 400km)$, to parts of the upper mantle.

As it is easy to observe from the figure set 4.3, a small change of the shear velocity in the superficial layers of the model, like the increase of 2.5%, carries out a significant variation on the phase velocity curve, especially in the high-frequency part of the range $(0.08 - 0.2)$ Hz.

For the intermediate domain, the change is well-observed at the low frequencies $(0.02 - 0.08)$ Hz, while a velocity change in the last domain does not contribute at all to the dispersion curve.

Regarding the other two parameters, Vp and ρ, a change in their profile will not contribute appreciably to a potential variation of the dispersion curve.

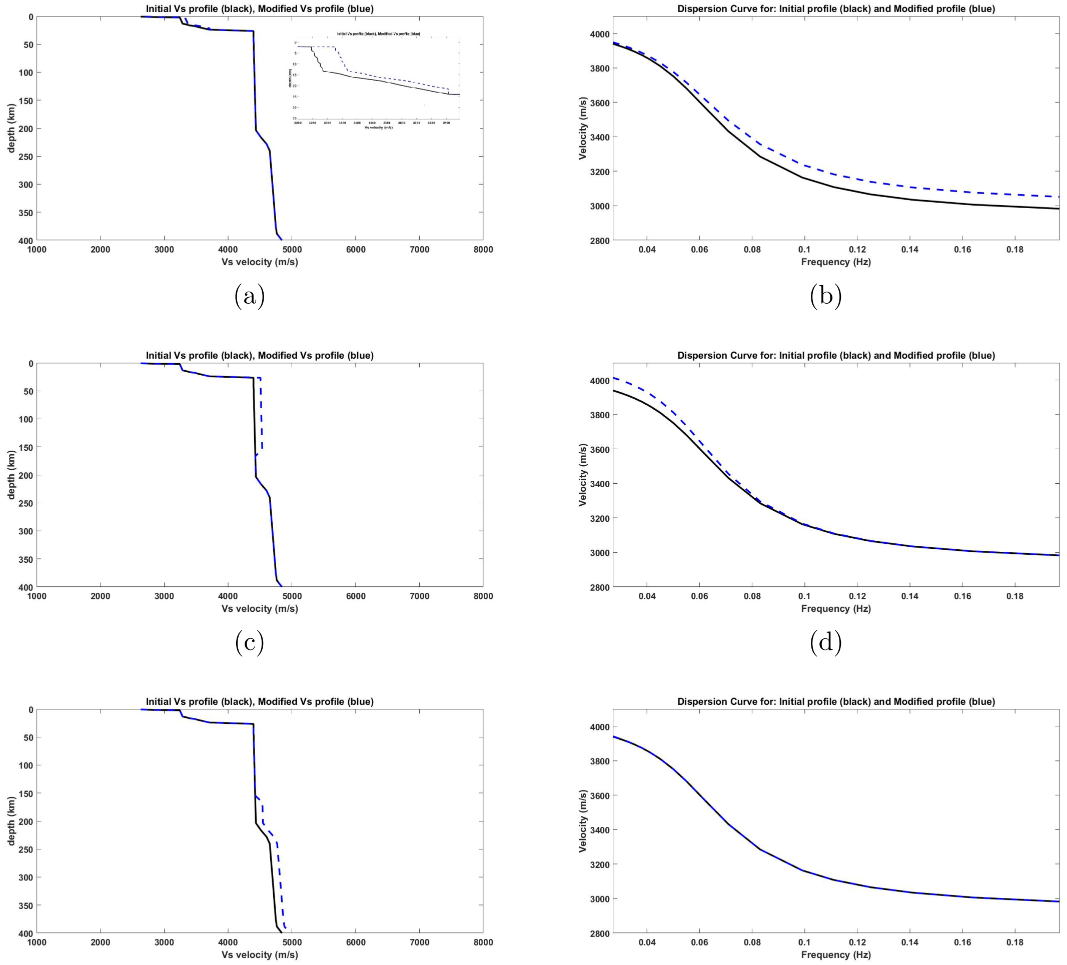

(a) (b)

(c) (d)

(e) (f)

Figure 4.3: Shear velocity variation in three different depth domains and the effect on Rayleigh phase velocity. Every couple of the subfigures correspond to an increase of the values of Vs in the domain $(0 - 24)$ km, $(24 - 150)$ km and $(150 - 400)$ km respectively. The blue dashed line indicates the variation.

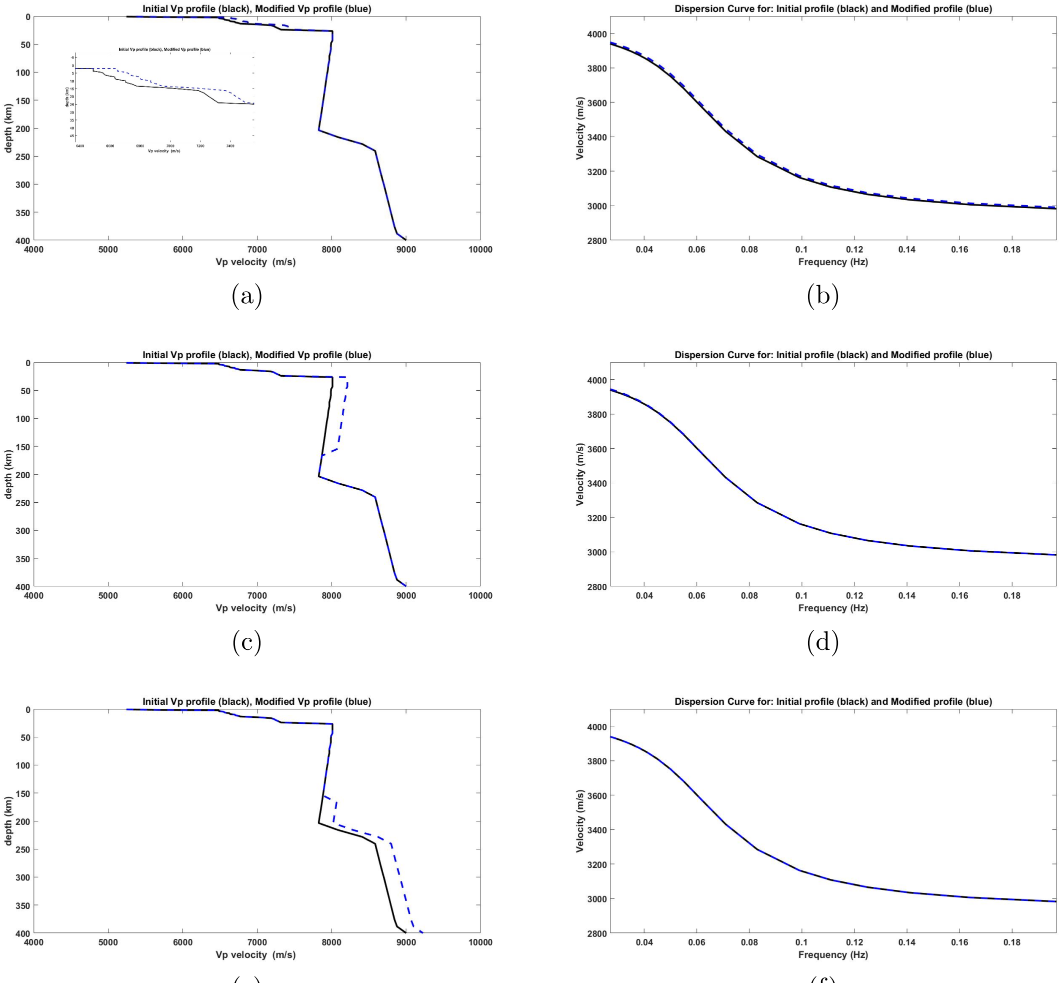

(a) (b)

(c) (d)

(e) (f)

Figure 4.4: Longitudinal velocity variation in three different depth domains and the effect on Rayleigh phase velocity.Every couple of the subfigures correspond to an increase of the values of Vp in the domain $(0 - 24)$ km, $(24 - 150)$ km and $(150 - 400)$ km respectively. The blue dashed line indicates the variation.

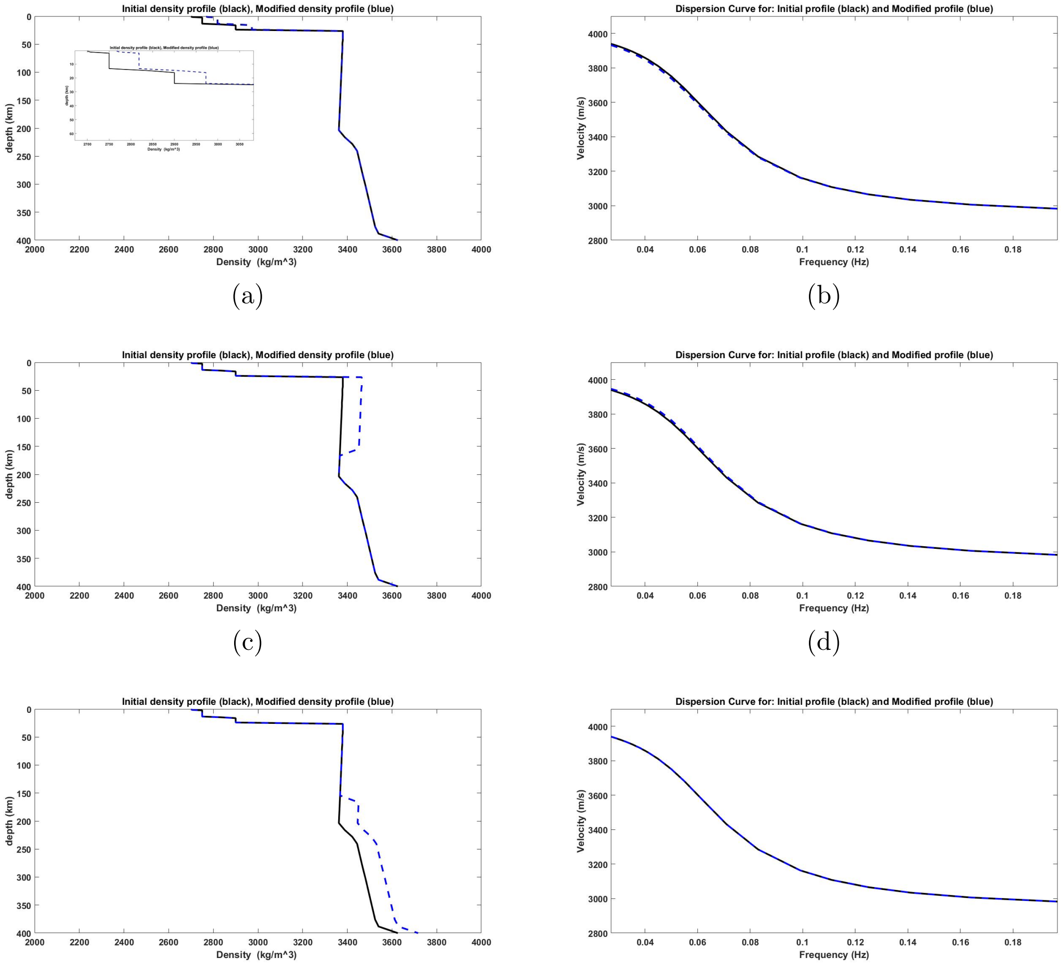

(a) (b)

(c) (d)

(e) (f)

Figure 4.5: Density variation in three different depth domains and the effect on Rayleigh phase velocity. Every couple of the subfigures correspond to an increase of the values of ρ in the domain $(0 - 24)$ km, $(24 - 150)$ km and $(150 - 400)$ km respectively. The blue dashed line indicates the variation.

To summarize, a shear-wave velocity change will be mapped clearly on the Rayleigh wave phase velocity for a certain frequency range, which is connected to the depth range as well. This simple test verifies the well-known fact that Rayleigh waves are more influenced by the S-wave velocity than the P-wave velocity or density.

4.3 Synthetic tests for the Oceanic Crust

As mentioned at the beginning, the inversion method can be applied to retrieve models of the oceanic crust as well and so, in this section a series of tests performed in an arbitrary cell in North Pacific is presented. This case can be performed when ocean-bottom seismometers are available [8].

The initial model is CRUST 1.0 [9]. This model assigns, for each 1°x 1 °a vertical profile of the model parameters, which are the body waves velocity Vp and Vs in

(km/s), the density ρ in (g/cm^3), the thickness of each layer in km, the Lamé parameters μ, λ and the Young's modulus E in GPa and Poisson's ratio ν. This is a global crustal model and as such, it provides an eight-layer crustal profile (water, ice, sediments, upper crust, etc) together with an uppermantle layer.

An arbitrary point was selected near Hawaii for synthetic testing. The target model used for generating the data was one created with shear-wave velocity values faster than those of the a priori model and the discontinuities kept the same but in shallower depth. Then, a fixed Vp/Vs ratio is defined ($= 1.7321$) in order to find the velocity of the P-waves. Regarding the density values, I use the Gardner relation [25]

$$\rho = 309.6(Vp)^{0.25}. \tag{4.7}$$

So, both initial and target model consist of 3 homogeneous layers and the halfspace.

For simulating actual data, Rayleigh-wave phase velocities obtained by solving the forward problem with the target model as input are corrupted with 1.5% of Gaussian noise. The smoothness scale value used for these tests is 5000 m.

Using this approach of inversion, the inverted model should represent the heterogeneities of the "real" model, while being guided by the a priori model. However, since the very beginning of the testing process with non homogeneous initial models, thus models with discontinuities, I have discovered that the inversion may recover models too close to the initial model, and not by the "real" one. In order to avoid this kind of behaviour, I use a polynomial fit of the a priori model, which is boxcar function-like. For the inversion of a stratified model, the Moho discontinuity between crust and upper mantle is important to be well-presented and so, in some of the tests below, I have defined it explicitly.

In all tests it has been added a 1 km of water layer above the solid medium in order to simulate the oceanic crust. However, the shear-wave velocity profile (in the following figures) determines the depth below the water-solid interface. The tests concern variations in the initial model, in the total thickness of the model and in the frequency range. They have been carried out as follows:

1. In the first two tests 78 fundamental mode and first overtone phase velocity measurements have been generated under the frequency range of (0.001 : 0.781) Hz. The layering is uniform with 900 elements of 250 m thickness each and so, the total thickness of the model equals 225 km. The difference is in the initial model.

    (a) From the dispersion curve in figure 4.6 (a) it can be observed that not all the data are used as for some frequencies the mode is non-guided. For instance, the low frequency range is missing for the first overtone, where the generated data appear at 0.2 Hz and the predicted data at 0.3 Hz.

    Regarding the shear-wave velocity profile (fig. 4.6 (b)) it seems that the recovered model (black), which is the last update of the inversion, represents the theoretical model (blue) but without mapping the discontinuities. Below the depth of the 10 km, the update model returns to the initial one (red).

Sensitivity kernels are plotted in figure 4.6(c), for the final inversion update: for the low frequencies the sensitivity is transferred to the fundamental mode for depths shallower that 5 km, while for the high-frequencies to the first overtone for the same depths. The kernels are similar for the intermediate frequencies.

(b) The difference of this test with the previous one is that the a priori model explicitly includes a discontinuity at 16.5 km, where, from the CRUST1.0, is located the Moho (figure 4.7 (a),(b),(c)).

In this case, the inverted model (black dashed) is constrained by the discontinuity and below it, reverts as expected to the initial model (red dashed) (fig. 4.7 (b)). The discontinuity can be also observed in the sensitivity kernel for the fundamental mode (fig. 4.7 (c)).

2. We will repeat the first set of tests by decreasing the range of frequencies, which is going to be (0.02 : 0.26) Hz. There are 120 measurements generated.

    (a) The plots (a), (b) and (c) in figure 4.8 are for the case of introducing an initial model which is smooth.

    As it can be seen by the plot of the dispersion curves (4.8 (a)), in this frequency range the overtone does not exist, and so the inversion is made only with the fundamental mode. This is why the recovered model is smooth and representative of the theoretical model (black dashed and blue in fig. 4.8 (b), respectively) for layers a little deeper than the 5 km depth. This can also be confirmed by the plot of the sensitivity kernel, where the sensitivity is large at that depth.

    (b) The Moho discontinuity is explicitly imposed (plots (a), (b) and (c) in 4.9), similarly to the second case of the test 1. There is still the instability under 5 km, but this time due to the existence of the aforementioned discontinuity at around 17 km, the inverted model returns to the theoretical model but maps the discontinuity at the same depth as the initial model.

    In both cases of the test 2, the inverted model is expected to revert to the initial model after some kilometers.

3. (a) For the last test in the oceanic crust the nonuniform layering, calculated in the way explained in section 4.1.1, represents the thin layer system and its spacing. Therefore, the computational grid consists of three parts, which are determined by the maximum and minimum sensitivity depths, z_{max} and z_{min}, respectively. The first is a uniform part of 10 elements with 700 m of thickness each, the second non-uniform part consists of 29 elements, whose thickness increase exponentially in to the range of (700m-$\sim$ 12 km) and the third uniform part of 24 elements of $\sim$ 12 km thickness each. The total thickness of the model is around 400 km.

    From the test set 2, it has been clear that there are no first overtone data for this specific range of frequencies and so, in the present case only fundamental mode data are included in the inversion.

The inverted model reconstructs the true model well down to a depth of more or less 30 km. Then, as already seen, resolution is lost and returns to the initial model (fig. 4.10 (b)).

In the case of the nonuniform layering, I plot the sensitivity kernel not as in tests 1 and 2 in a matrix form, where the rows represent the depth and the columns the frequencies, but for each frequency-column separately (4.10 (c)). Phase velocity at ~ 4 s is sensitive to variations of the S-wave velocity at depths around 5 km. At ~ 6 s Rayleigh waves sample the crust at a thickness of 10 km, while at ~ 8 s they are sensitive to a depth of $16-17$ km, and thus we may say that they contain information for the crustal part of the model. Under that depth, some sensitivity still exists nearly for 20 s, which suggests some influence from the upper-mantle part.

(b) This last test is repeated after changing the smoothness scale value and imposing it equal to 1000 m (fig 4.11 (a),(b) and (c)).

By comparing the plots of the two cases of the third test (4.10 (a), (b), (c) with 4.11(a), (b) and (c) equivalently), it seems that the first choice of the smoothness scale value, 5000 m, is better that the second one. The predicted data (black dots) fit better the theoretical data (blue dots), while the inverted model (black dashed in plot (b)) does not present the instability at the depth interval of $10-20$ km. There is no appreciable difference in the kernel plots.

This analysis leads to some important conclusions that will be considered for the inversion of the real data.

Initially, the inverted model is mainly guided by the a priori model. This is not so surprising when using a linearised inversion approach, but still it is considered as a problem when global reference models with large shear-wave velocity discontinuities, like CRUST1.0, are used as initial models, since there cannot be retrieved a good representation of the real Earth.

Second, for a low-frequency range, there are only fundamental mode data.

In addition to this, the predicted data (black dots) fit well the real (synthetic) data (blue dots), especially for the higher frequencies. The low-frequency predicted data do not seem to follow the trend of the equivalent “real” data. To fit better the low frequencies, an appropriate smoothness scale should be used.

To conclude, using the nonuniform layering has definitely provided with shorter execution times for the codes. This is essential when the inversion process is made in big datasets, with the aim of obtaining 3D shear-wave velocity structures.

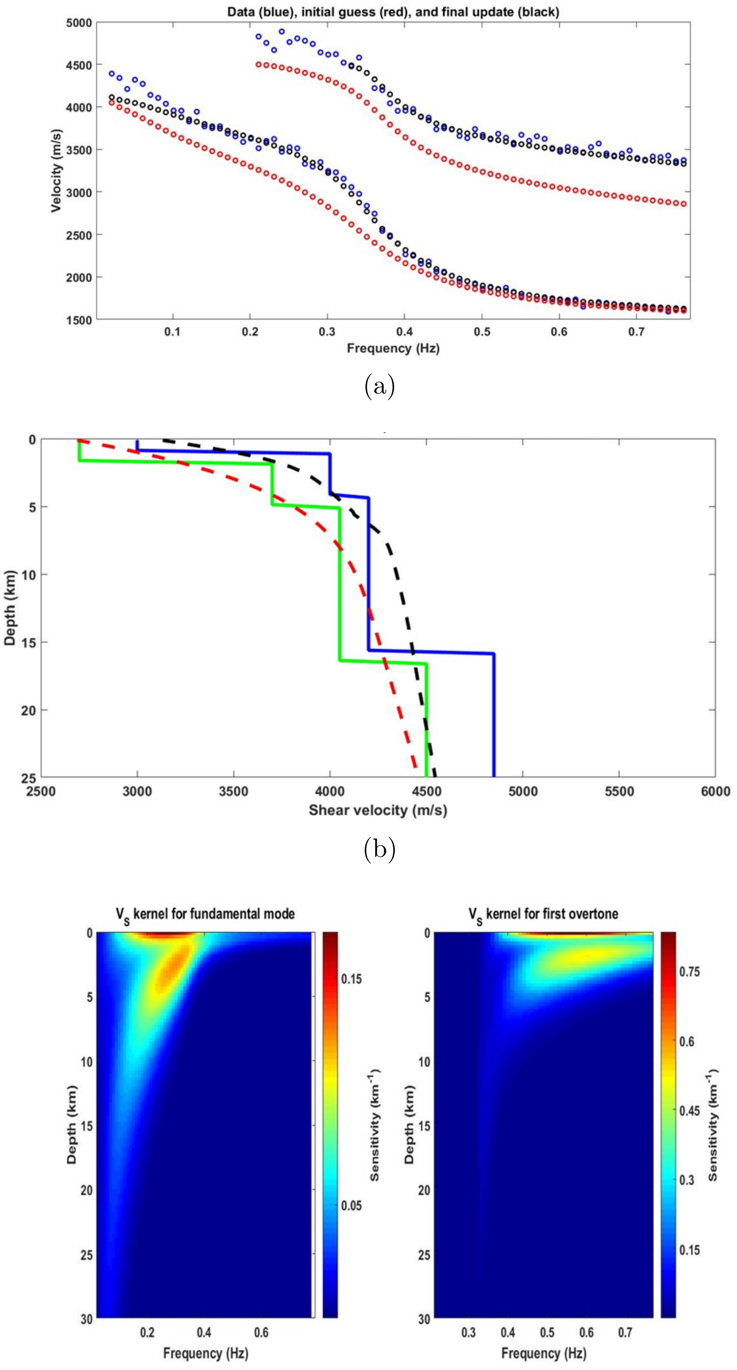

(a)

(b)

(c)

Figure 4.6: (a) Dispersion curves for the fundamental and first overtone data (blue), initial model (red) and predicted data from the inversion (black). (b) Shear-wave velocity profile for true model(blue), initial model (red dashed, which is the polynomial fit of the green) and the last update of the inversion (black). (c) Sensitivity kernels for the fundamental mode and first overtone. The frequency range is (0.001-0.781) Hz.

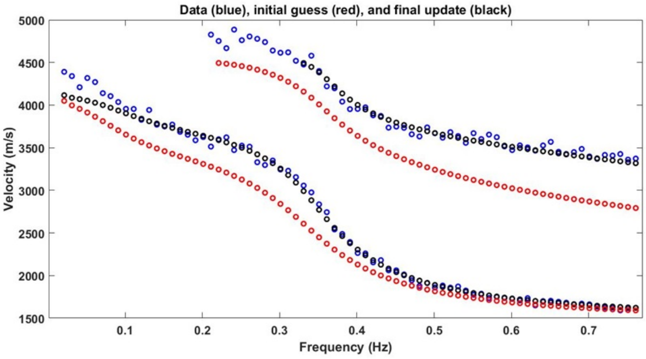

(a)

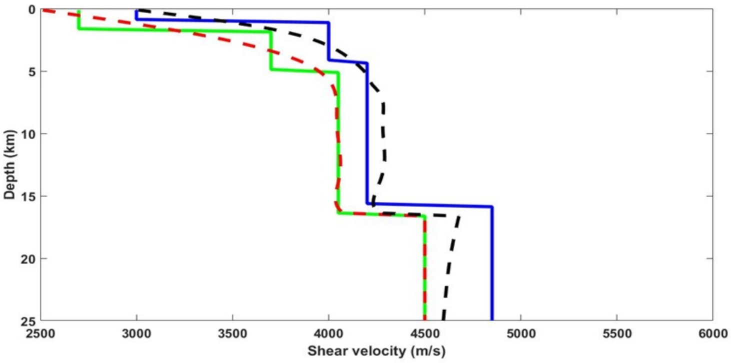

(b)

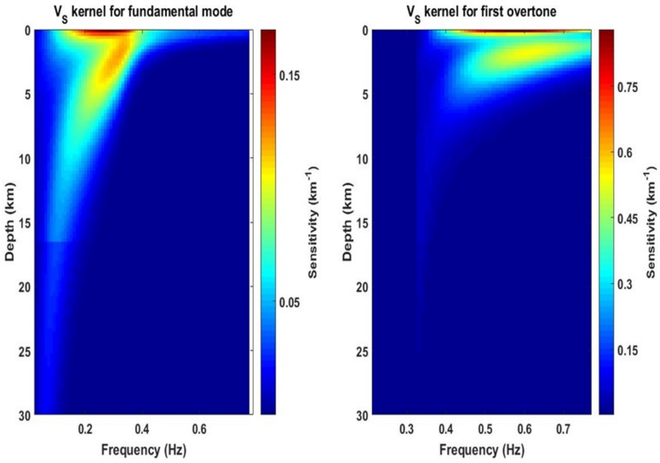

(c)

Figure 4.7: (a) Dispersion curves for the fundamental and first overtone data (blue), initial model (red) and predicted data from the inversion (black). (b) Shear-wave velocity profile for true model(blue), initial model (red dashed, which is the polynomial fit of the green) and the last update of the inversion (black). (c) Sensitivity kernels for the fundamental mode and first overtone. The frequency range is (0.001-0.781) Hz.

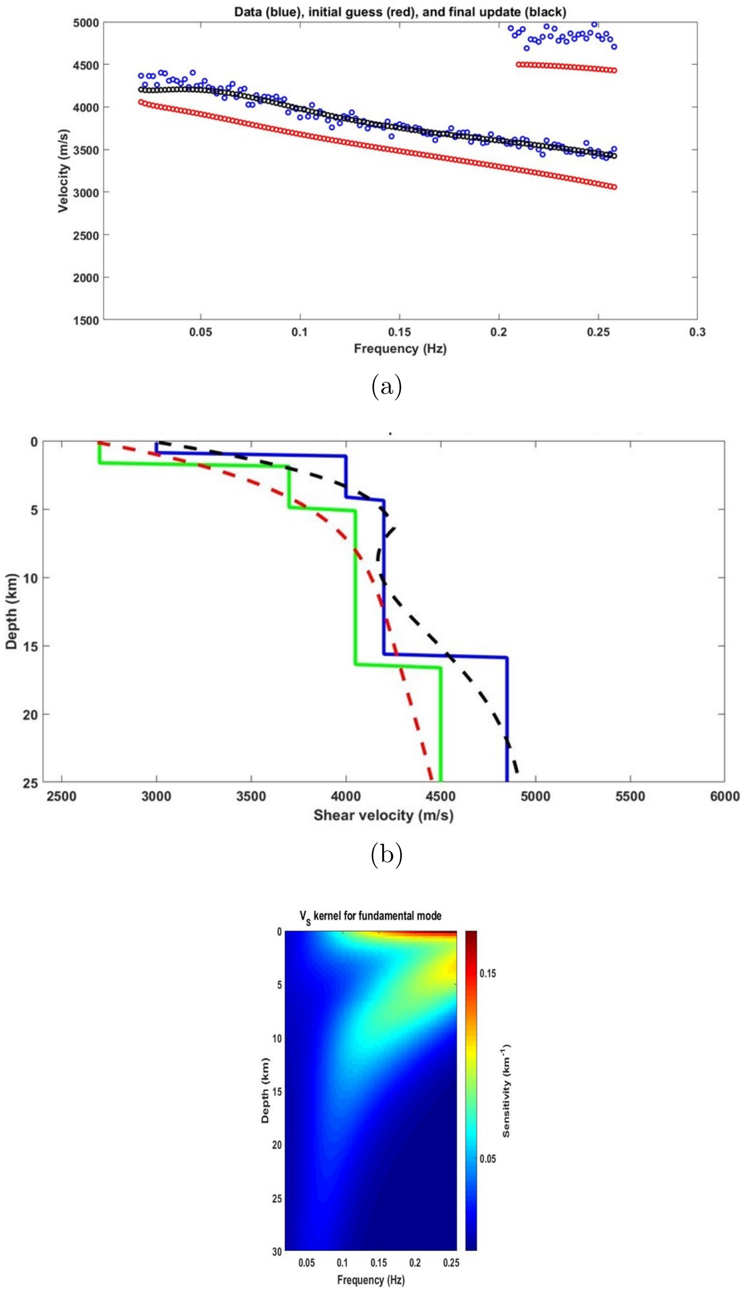

(a)

(b)

(c)

Figure 4.8: (a) Dispersion curves for the fundamental and first overtone data (blue), initial model (red) and predicted data from the inversion (black). (b) Shear-wave velocity profile for true model(blue), initial model (red dashed, which is the polynomial fit of the green) and the last update of the inversion (black). (c) Sensitivity kernel for the fundamental mode. The frequency range is (0.02-0.26) Hz.

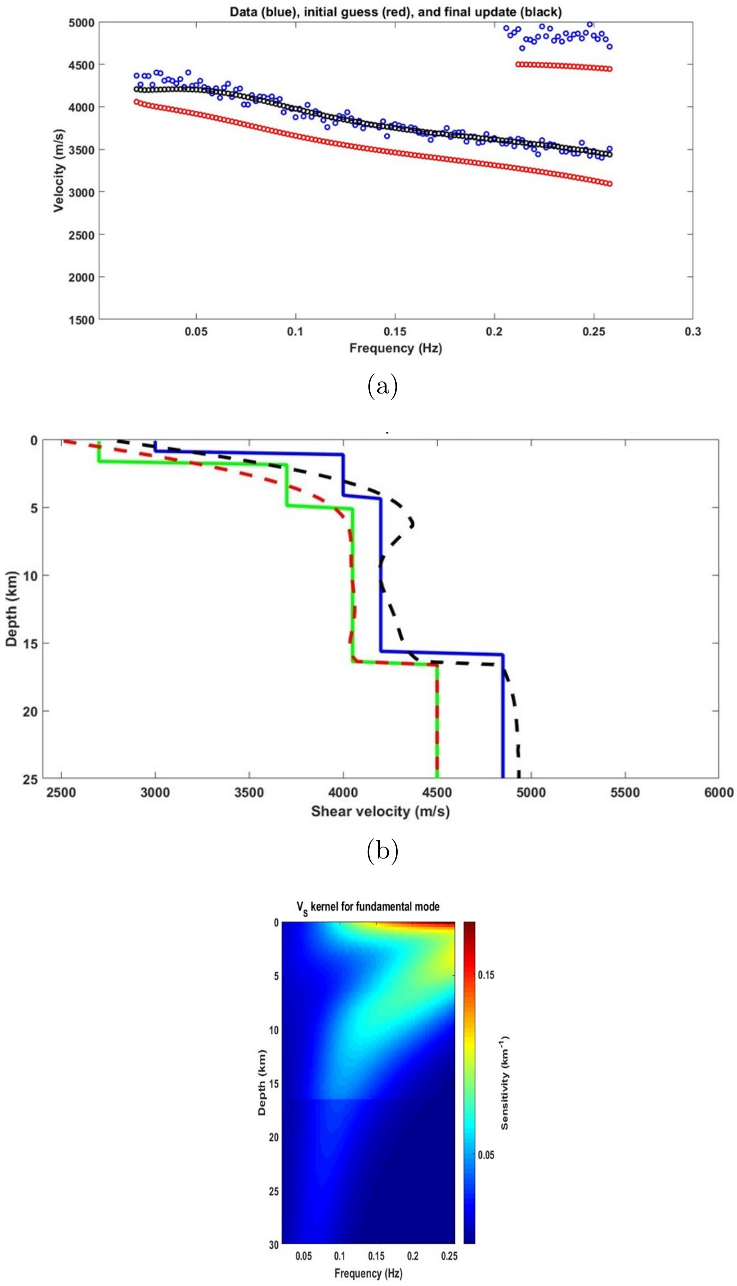

(a)

(b)

(c)

Figure 4.9: (a) Dispersion curves for the fundamental and first overtone data (blue), initial model (red) and predicted data from the inversion (black). (b) Shear-wave velocity profile for true model(blue), initial model (red dashed, which is the polynomial fit of the green) and the last update of the inversion (black). (c) Sensitivity kernel for the fundamental mode. The frequency range is (0.02-0.26) Hz.

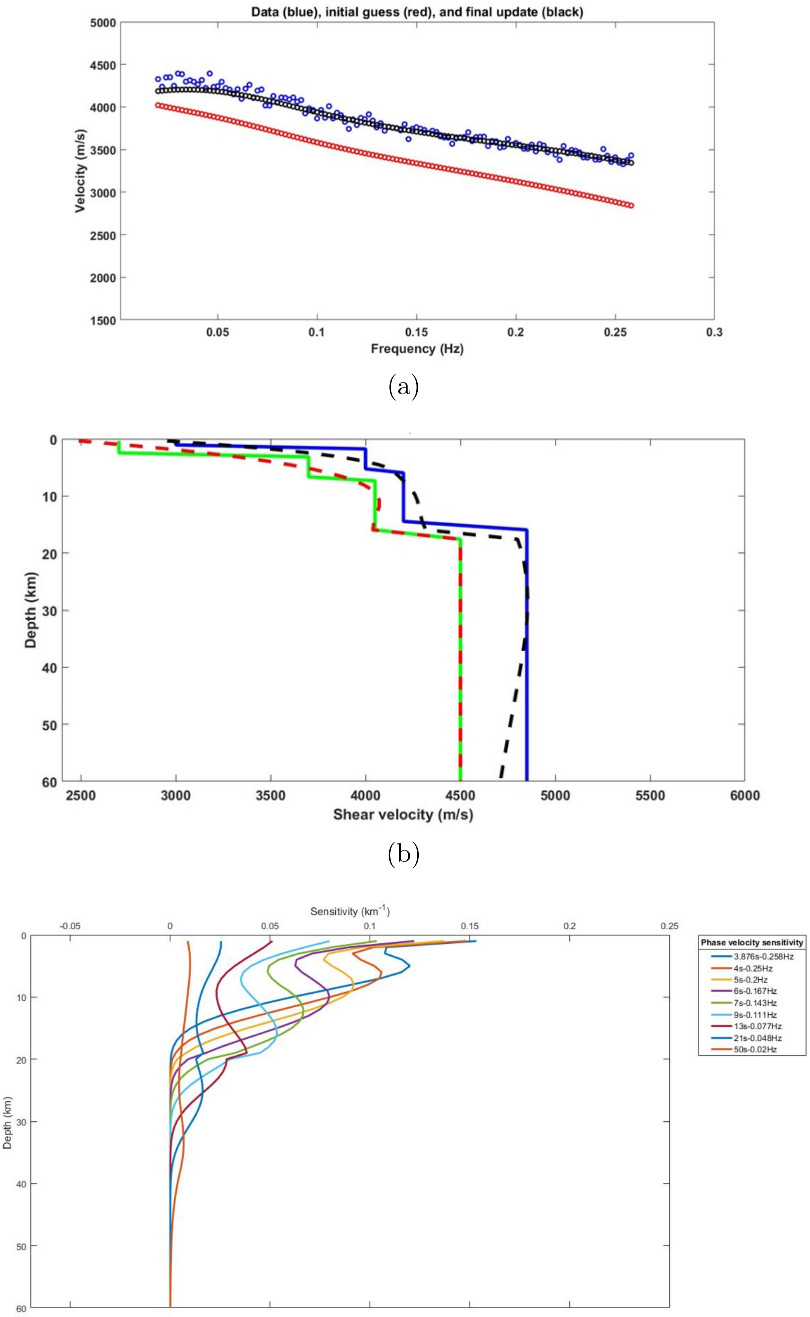

(a)

(b)

(c)

Figure 4.10: (a) Dispersion curves for the fundamental data (blue), initial model (red) and predicted data from the inversion (black). (b) Shear-wave velocity profile for true model(blue), initial model (red dashed, which is the polynomial fit of the green) and the last update of the inversion (black). (c) Sensitivity kernel for the fundamental mode. The curves correspond to 3 s, 4 s, 5 s, 6 s, 7 s, 9 s, 13 s, 21 s, 50 s from shallow to deep depths.

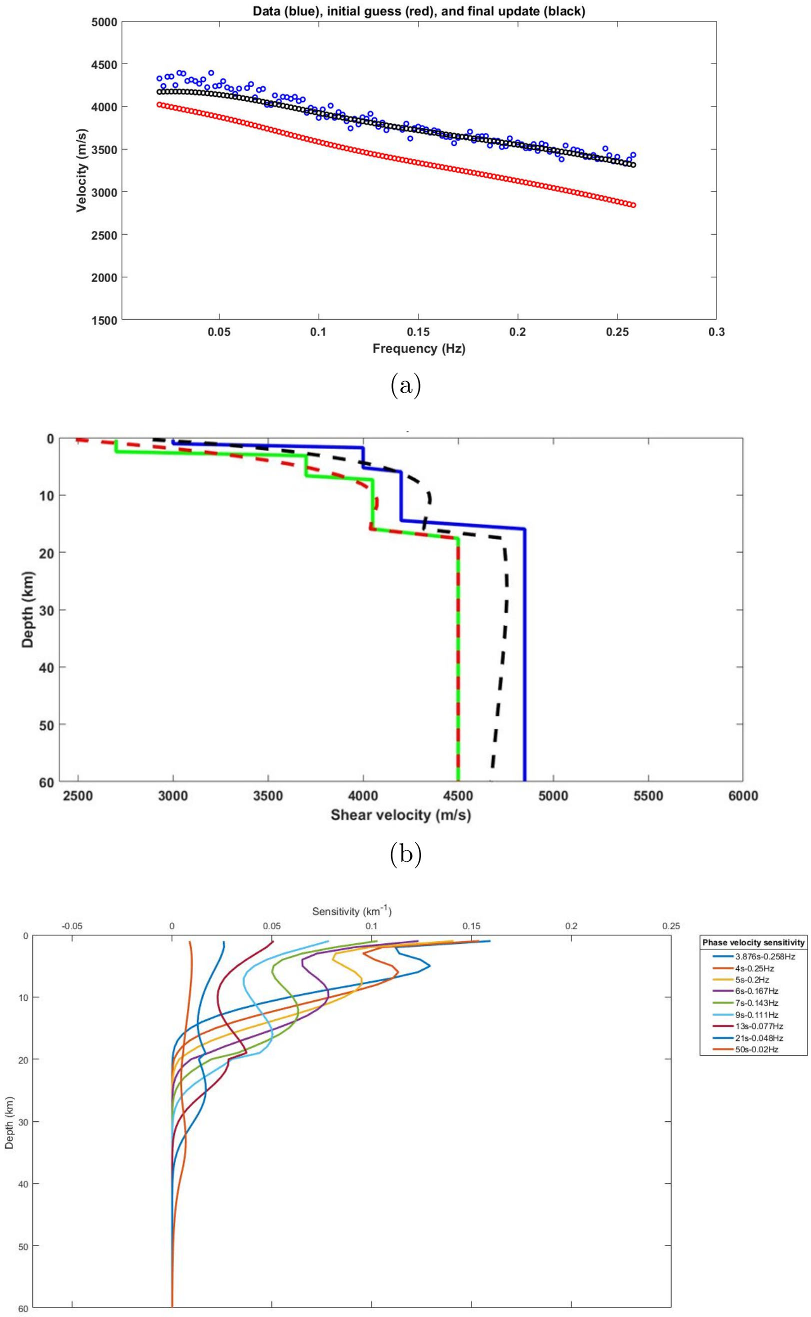

(a)

(b)

(c)

Figure 4.11: (a) Dispersion curves for the fundamental data (blue), initial model (red) and predicted data from the inversion (black). (b) Shear-wave velocity profile for true model(blue), initial model (red dashed, which is the polynomial fit of the green) and the last update of the inversion (black). (c) Sensitivity kernel for the fundamental mode. The curves correspond to 3 s, 4 s, 5 s, 6 s, 7 s, 9 s, 13 s, 21 s, 50 s from shallow to deep depths.

Chapter 5

Perturbational inversion applied to Italy

5.1 Ambient noise database

In chapter 4, I have presented the results of synthetic data inversion, simulating the oceanic crust. In this chapter, I repeat the process for fundamental mode phase-velocity data from seismic ambient noise. The database that I use, is the one from the work of Molinari et al. [2], where cross-correlation of the vertical component of seismograms recorded for 1 year at stations all over the Italian peninsula and the Alps, has been made as explained in the aforementioned article (figure 5.1). In order to obtain phase-velocity data, they apply the two-station method for every available station pair that belongs to the network. In this way, they obtain data within the period range of 5-37 s. The parametrization of the region remains the same and it is divided in 0.25°x 0.25°cells.

Ambient noise, which constitutes a random wavefield over sufficiently long times, is composed by surface waves [26], [27]. In short period band (<20 s), also known as *microseisms*, is the product of the interaction of the swells [1] with the ocean floor in the vicinity of the coastlines. The two strongest peaks in the short period band are the primary (10-20 s) and the secondary (5-10 s). The primary microseisms are related to the interaction of the water waves with the shallow ocean floor, which can be represented by forces (friction on the ocean bottom in horizontal and pressure on the surface of the sea in vertical) that generate the ambient noise, which is made of Scholte surface waves. The secondary microseisms is the product of two same frequency primary microseisms, that propagate in the opposite direction. This is a nonlinear interference phenomenon, that can take place, again but not only, near the coast where the direct and the coast-reflected waves meet.

From the cross-correlation of ambient noise records from two stations, one may estimate the Green's function between the stations, which provides information on the propagation properties of the wavefield [26].

In the following sections, I present shear-wave velocity structures using two different a priori models. In the simplest case (5.2, 5.3) the inversion is made with an

---

[1] a ocean swell is a gravity wave generated by a distant weather system, and as such can propagate along the interface of the ocean and atmosphere for long distances, if not dissipated.

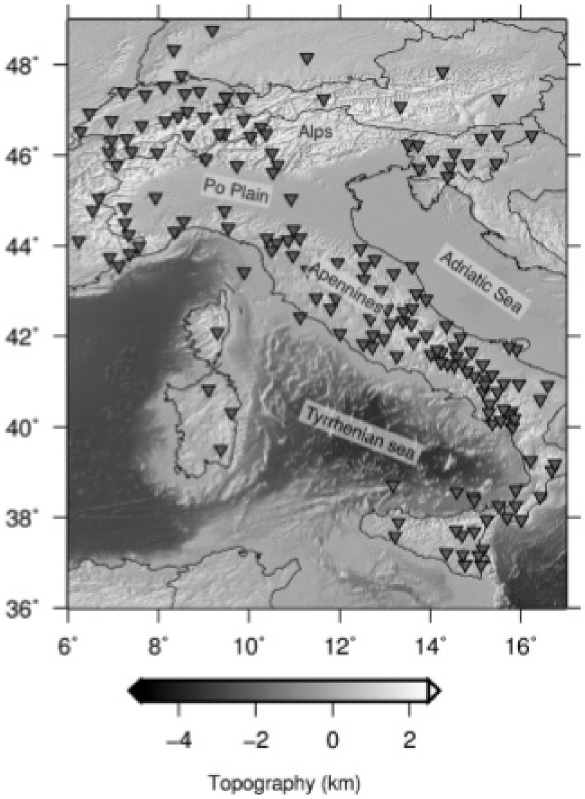

Figure 5.1: Stations where the seismograms were recorded.(After Molinari et al. [2])

initial model that was generated on the basis of the same data that I use in this work. Subsequently, in section 5.4, I apply the inversion method in some test cases, taken from the same database, but this time the a priori model is based on the Dix-type inversion.

5.2 One-Dimensional shear velocity profiles

Before applying the linearised inversion to the entire desired region (Italy and Alps), I implemented the inversion approach to a few sample cases as tests, and in the present section I present two of them.

The a priori model at the crustal part is the average of the 500 best-fitting solution models, resulting from the inversion made by Molinari et al. [2]. Their inversion is a stochastic direct search applied by the Neighbourhood Algorithm [28], [29], and so a number of possible solution models is retrieved. For the mantle, the model parameters are the PREM model values [3].

The 1D layering and the smoothness scale are calculated as described in the previous chapter. The element thicknesses are exponentially increased with depth (section 4.1.1) and the smoothness scale follows that increase as well (section 4.1.2). The a priori model is fitted to the nonuniform grid. The Vp/Vs ratio is not maintained fixed during the inversion.

The frequency range of the phase velocity is $0.027 - 0.2$ Hz. Not all of the data exist for the entire range though.

In order to calculate the standard deviation of the data, and so the covariance matrix, I generate data in the same range frequency with the real ones and corrupt them with 1% of Gaussian noise. The model parameters are the same with those used in the inversion.

The standard deviation of the model, necessary for the calculation of the covariance matrix, is imposed to be larger by 30% of the mean value of the standard deviation of the data.

In figures 5.2 and 5.3, I present the 1D shear-wave velocity structure (b), the phase-velocity dispersion curves (a) and the sensitivity kernel (c) of two cells/cases in Northern Alpine area and North Italy. The first three subfigures correspond to the place with geographic coordinates (48°N, 9°E) which is located at the north of the Alps (figure 5.2), while the rest of them in figure 5.3 correspond to (46.25°N, 10.75°E) in the Alpine belt. These cells correspond to examples of foreland basin and orogenic crust, respectively (points C and E in figure 5.8).

With respect to the case of the Northern Alpine foreland, we can see that the predicted data from the inversion result(black dots) fit well the data (blue dots) for the range frequency of $0.08 - 0.197$ Hz, while there is a small difference between the curves for the lower frequencies (fig 5.2(a)). The update model, black dashed in 5.2(b), follows the exact same trend of the initial model (red dashed) for the superficial layers. For depths below the fifth km, the update model differs from the initial and becomes slower for the depth domain of $10 - 27$ km, where below that is the Moho depth. Below the Moho depth at 30 km, the update model reverts slowly to the initial one. In the subfigure (c) the sensitivity kernel for a number of frequencies are plotted. As expected, in general shallow depths influence the high frequency Rayleigh waves, while the deeper structures dominate at low frequencies. In this case, I suggest that the Rayleigh waves of the period range $(\sim 5 - 37)$s are sensitive to a depth domain of ~ 6 km down to ~ 30 km accordingly, which represent in the chosen parametrization the upper crust and some layers in the upper mantle. The three sensitivity kernels representing the low frequency range are not smoothed, reflecting the discontinuity between the 20 and 30 km.

A similar analysis can be made for the case of the Alpine orogen crust, where the frequency range of the data is $0.164 - 0.027$ Hz. The fit of the data (blue dots) by the predicted data from the inversion (black dots) presents a deviation at the low frequencies 5.3 (a), in this case as well. In the figure 5.3 (b), the update model (black dashed) deviates from the initial one (red dashed) in the depth range of $(\sim 10 - 40)$ km, while deeper returns to it. Shallow structures at around 10 km depth dominate at high frequencies, like 0.164 Hz, while at lower frequencies 0.027 Hz, Rayleigh waves are more sensitive to deeper structures, like those that appear in the upper mantle.

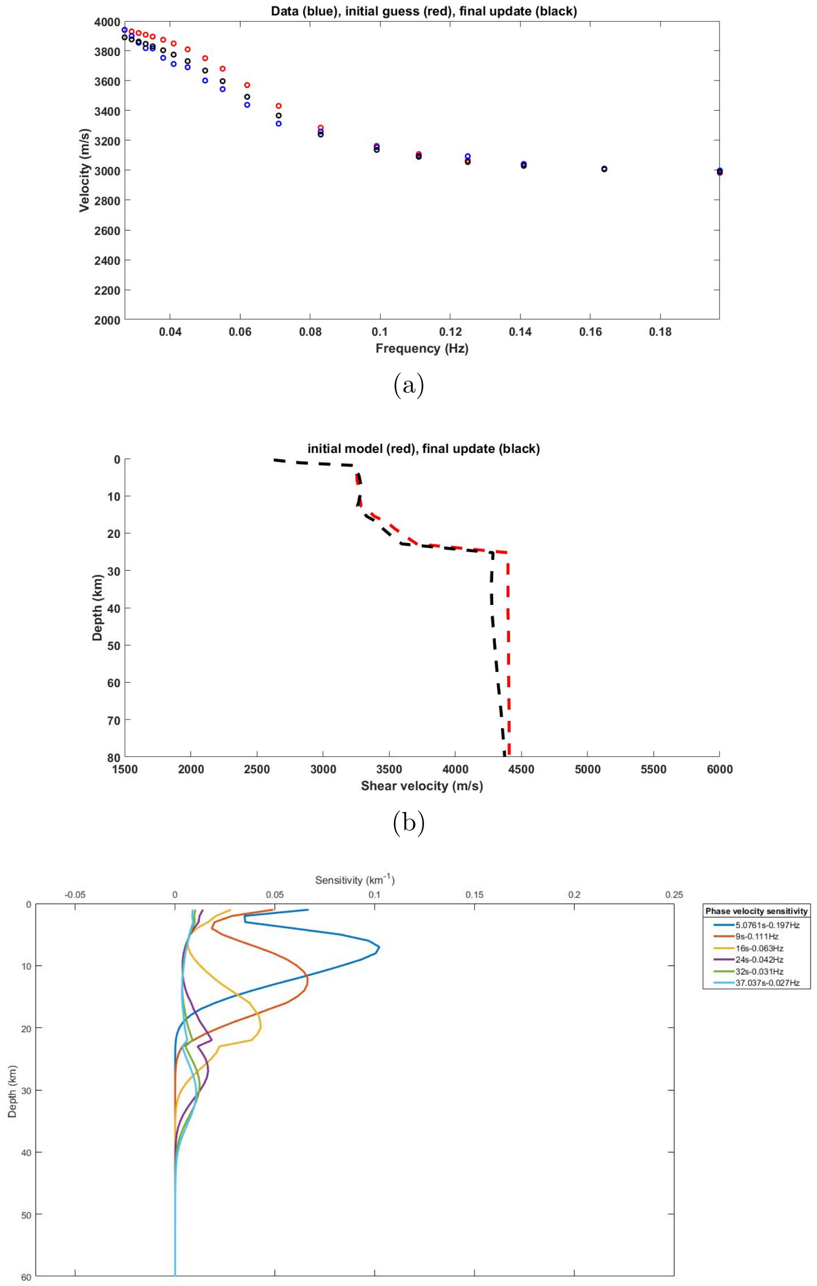

(a)

(b)

(c)

Figure 5.2: (a) Dispersion curves for the fundamental mode data (blue), initial model (red) and predicted data from the inversion (black). (b) Shear-wave velocity profile for true model(blue), initial model (red dashed, which is the preferred model in figure 5 of Molinari's et al. work [2]) and the last update of the inversion (black). (c) Sensitivity kernel for the fundamental mode. (Northern Alpine foreland case)

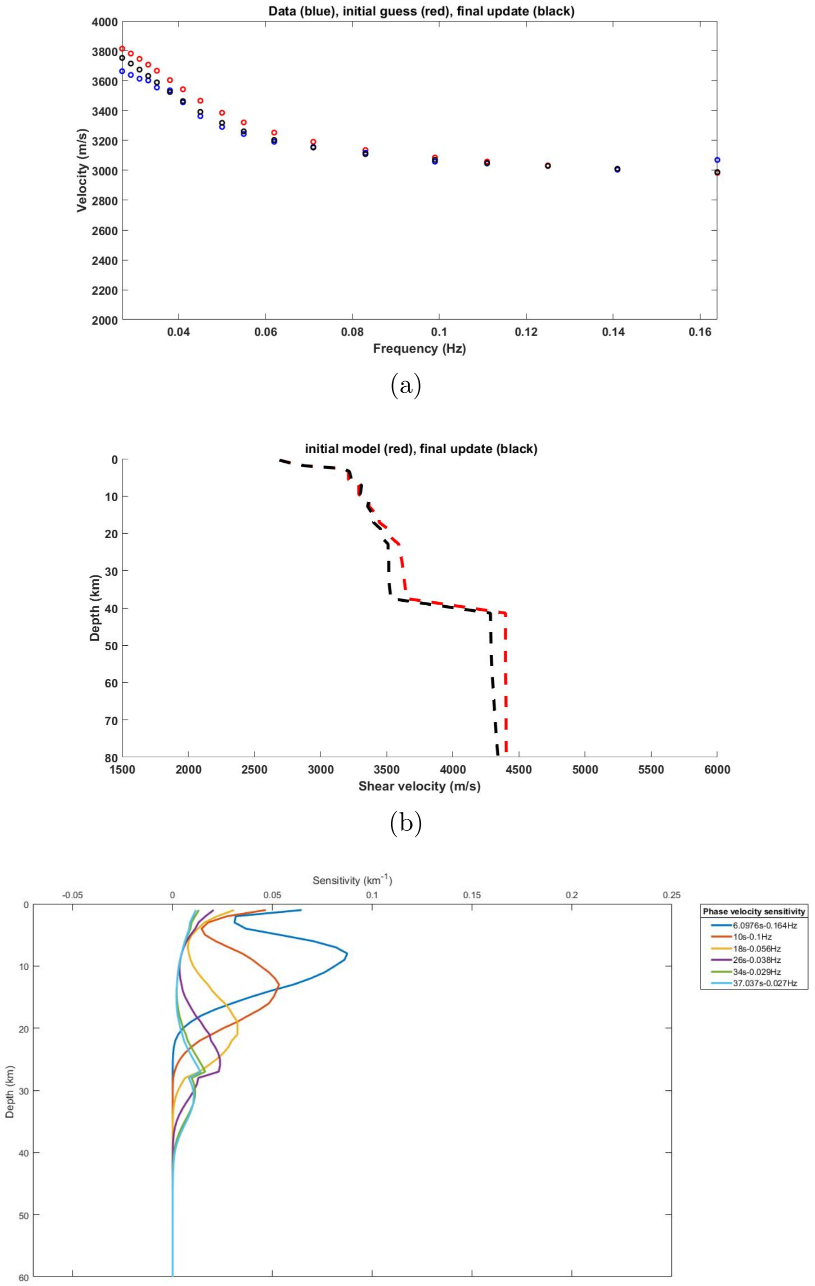

(a)

(b)

(c)

Figure 5.3: (a) Dispersion curves for the fundamental mode data (blue), initial model (red) and predicted data from the inversion (black). (b) Shear-wave velocity profile for true model(blue), initial model (red dashed, which is the preferred model in figure 5 of Molinari's et al. work [2]) and the last update of the inversion (black). (c) Sensitivity kernel for the fundamental mode. (Alpine orogen crust case)

5.3 Three-dimensional shear velocity structure

In order to study the three-dimensional shear-wave velocity structure in the desired region, I repeat the inversion process described above (section 5.2) to a number of cells, which are located in the domain of (6°-16.25°)N and (36.75°-51°)E (figure 5.1).

The space is parametrized with layers that fit the nonuniform layering and the smoothness scale matrix increases with depth, as already described. Since the calculation of the computational grid spacing is based on the minimum and maximum wavelength of the data, I find the equivalent values in five representative cases all over the area, and define a unique layering for all data points. In this inversion scheme, the data covariance matrix is calculated in the same manner as in 5.2, but this time I added 1.5% Gaussian noise, instead of 1% in the previous case. The model standard deviation factor is also different, as I imposed it equal to twice the mean value of the standard deviation of the data. Since the changes are small, they should not noticeably affect the output.

The a priori model remains the same, as in the previous section. For each cell I use the average of the 500 best models as intial model, provided by the work of Molinari et al. [2].

The number of geographic points, that determine the vertical shear-wave velocity map projection, surpasses the 1400. The regions covered by the cells are regions of central and north Italy, together with parts of the Alpine countries: France, Switzerland, Germany and Austria. Ligurian and Tyrrhenian sea are also visualised, mostly near the italian west coast. The phase velocity dataset is at frequencies between 0.027 Hz and 0.2 Hz.

Figures 5.4 and 5.5 represent the shear-wave velocity maps at different depths. In order to visualize better the velocity differences as the depth increases, the scale is different in the two figures.

The superficial part of the crust, together with a sedimentary layer, is presented at the depth of 3 km. The two Alpine foreland basins are well-distinguished with shear-wave velocity values ranging in the domain of $2 - 2.5$ km/s. More precisely, at the Northern Alpine basin the low shear-wave velocity values expand in parallel of the northern part of the Alps, while at the southern part where the Po Plain is located, there are low velocities ($\sim$ 2km/s) at the part of the Adriatic sea and higher ($\sim$ 2 km/s) at the other part. This comes into contradiction with Molinari et al.[2], since they have presented higher velocity values at the Northern part and uniform low velocity values across the Po Plain basin. At that depth, the high shear-wave velocity also starts to reveal at the two mountain ranges, the Alps and the Apennines. The difference in the velocity can be seen better in the case of the Alps. The velocity remains low at the part of the Ligurian and Tyrrhenian sea.

Increasing the depth, at 4 and 7 km the differences in shear velocity remain, as there are low values in the Po Plain basin and the Tyrrhenian sea, while higher values are mapped across the Alps and the Apennines. The map at 4 km section seems to be more consistent with the equivalent map of the 3 km at the work of Molinari et al. [2], mainly at the Molasse basin.

The upper crust can be visualised at a depth of 10 km. Even in this depth, it can be seen the variabily of the velocity in the places mentioned above. This is in good agreement with Molinari et al. [2]. The shear-wave velocity in the basin north of the Alps takes values around the 3.2 km/s, while the Po basin presents values ranging from $2.6 - 2.8$ km/s. This is an evidence of the different evolutionary history of the two basin around the Alps.

In the next figure (5.5), the maps at depths 20, 22, 29 and 36 km are presented.

At the depth of 20 km, there are low velocity values at the two mountain ranges (Vs $\sim$ 3.2 km/s) while the velocity increases more smoothly than before, across their edges. At the part of Northern Alpine basin the shear-wave velocity takes values around $\sim$ 3.7 km/s and at the part of South Tyrrhenian and Ligurian sea the velocity arrives at 4.5 km/s, which is a clue that the Moho has been reached. The high velocity structure at the center of the Apennines is well-imaged, as it is the western part of the Po basin.

The map at 22 km preserves the same velocity anomalies to a lower degree, as it is expected. High velocity values dominate at the east part of the Italian Peninsula, the west part of Po Plain and the South-West Germany.

The map in 5.5 (c) represents the 29 km depth, which at the west and north part of Italy maps the upper mantle. In these places, the velocity ranges between $4.2 - 4.5$ km/s, while still the pattern of low velocity values at the two mountains (Alps and Apennines) and higher velocity values at the around basins (Po Plain and Molasse basin) remains. The Moho discontinuity at these two places has not been reached yet.

The last map (5.5 (d)) at 35 km depth is connected to the Moho depth. Overall, the resulting shear-wave velocity values are equivalent with the ones presented for the same depth at the work of Molinari et al. [2]. The only difference that I find is that the high velocity regions (Vs >4.2 km/s) are masked and the discrepancies presented in the aforementioned article, do not seem to appear in the present map. This indicates some loss of resolution, which was expected after doing the first tests in section 5.2.

In this work, I have found, in total agreement with Molinari et al. [2], for the oceanic crust (Tyrrhenian and Ligurian sea) the low velocity values for depths down to 10 km, while at the 20 km reveals the upper mantle structure. The Alps and the center of the Apennines maintain their crustal structure down to the depth of 36 km, which can be imaged by the low velocity values at the same depth. The Po Plain and the Northern Alpine foreland, at the upper crust depth, have values greater than the mountain belts. The only noticeable difference between the two works is in the uppermost part of the crust, where, in the present work, the velocity values at the two basins, and mainly at the Po Plain basin, are not uniformly distributed in the areas. It appears that the resolution is not sufficient at that depth.

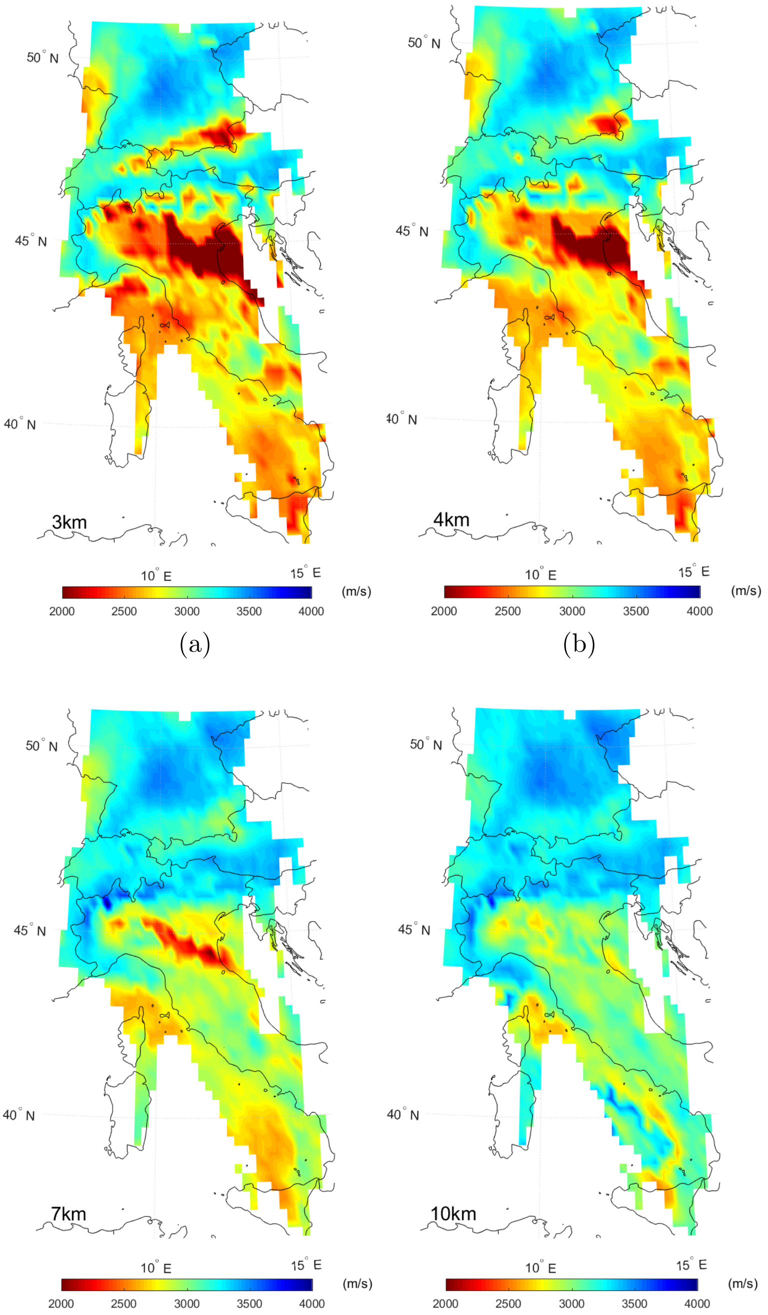
50° N
45° N
40° N
3km
4km
7km
10km
10° E
15° E
2000
2500
3000
3500
4000
(m/s)

(a) (b) (c) (d)

Figure 5.4: Shear velocity maps at depths (a)3 km (b) 4 km (c) 7 km and 10 km.

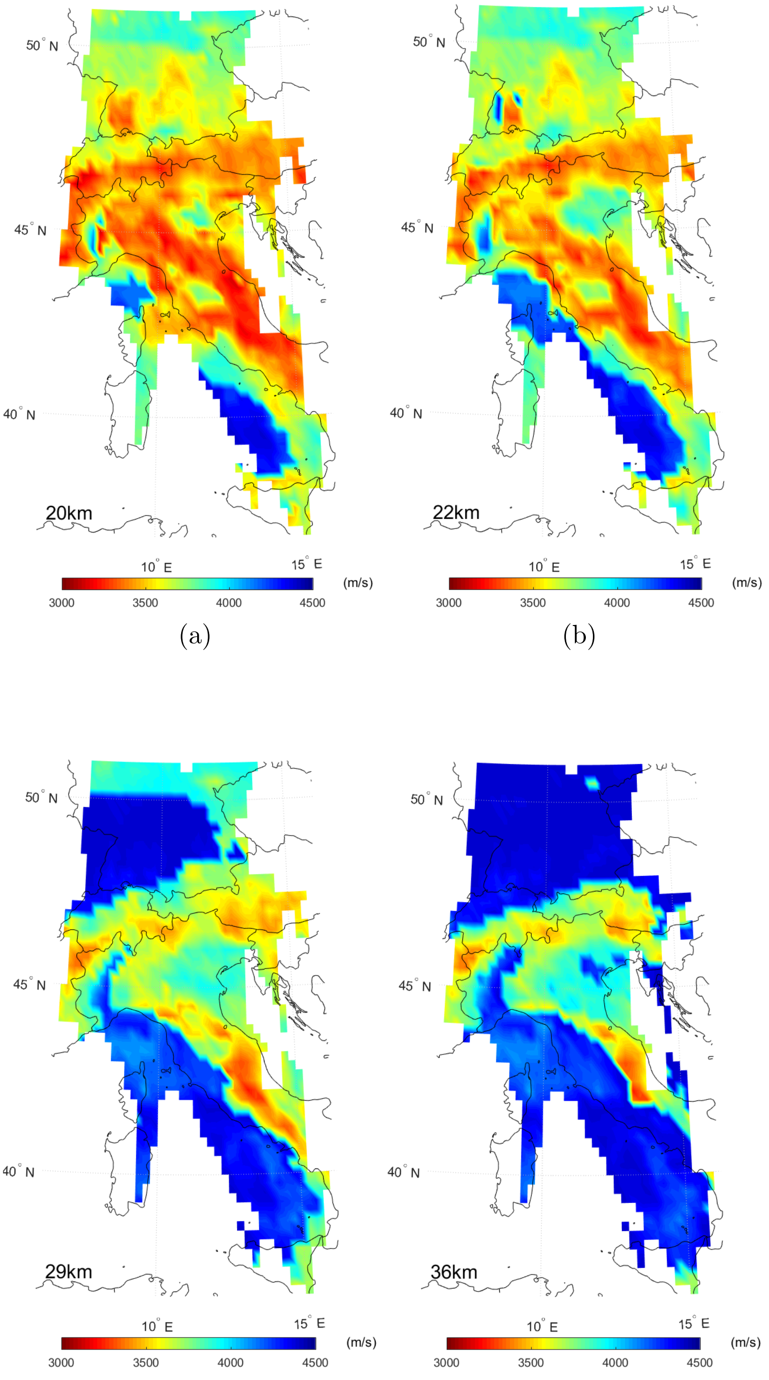

(a) (b)

(c) (d)

Figure 5.5: Shear velocity maps at depths (a)20 km (b) 22 km (c) 29 km and 36 km.

In order to conclude this chapter, I present the vertical section of the resulting, from the inversion, model (figure 5.6). It is a N-S profile that extends from 43°N 12°E to 49°N 12°E (figure 5.7) and practically crosses part of the Eastern Alps. This kind of profile is an other way of "visualizing" the shear-wave velocity structure as it reveals a complete image of the structure and its differences in depth.

In this case, it is well-distinguished a small part of the North Apennines, the Po Plain, the Alps and the Northern Alpine foreland. Under the Alps the shear velocity structure evolves more uniformly than it does under the two basins. The Moho depth extends from $25 - 30$ km under the basins, while under the Alps arrives at 40 km. This is also implied by the low velocities at a depth of 36 km in figure 5.5 (d), which means that this depth is still part of the low crust for the Alps.

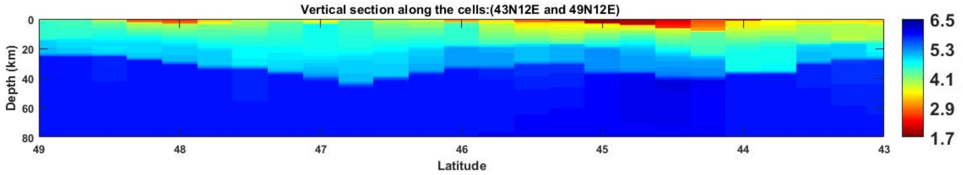

Figure 5.6: Vertical section starting from central Italy (B) up to South Germany (A). The distance is about 700 km. (1°corresponds to 96 km)

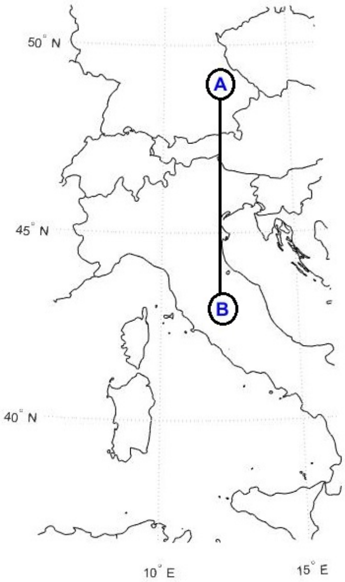

Figure 5.7: The two points A and B that set the limits to the vertical section presented in 5.6.

5.4 A priori model based on the Dix-type inversion

So far, I have had the opportunity to use a reliable a priori model, either because I was dealing with synthetic tests, or because I was using data that had already been inverted. Both of the cases constitute favourable circumstances, which may not always occur. Whenever that is the case, it is useful to devise an inversion strategy that does not rely on significant already established knowledge. This can be accomplished using a preliminary Dix-type inversion (as explained in section 3.3), to be used as initial model for the formal iterative inversion. Using the Dix-type method for inverting in order to obtain a satisfying initial model, first I have to settle some key parameters in order to build the layered model, as explained briefly in 3.3. This model is defined in a nonuniform layering, calculated in almost the same manner as 4.1.1.

The parameters that are user-supplied are the multiplicative coefficient between the wavelength and the sensitivity depth a, the number of layers per wavelength to be sampled in the sensitivity depth n and since the mapping of the data is made only between the range of minimum and maximum sensitivity depth (z_{min}, z_{max}), there is the need to introduce two multiplicative coefficients of the minimum and maximum layer thicknesses, that will determine the layer thicknesses and allow the model to extend to areas beyond that range. For the depth domain between surface and minimum depth of sensitivity $(0, z_{min})$ the coefficient is equal to 1, covering the area with uniform layers of thickness equal to the minimum thickness found in (z_{min}, z_{max}). For the depth domain of (z_{max}, ∞), the coefficient has to be >1, in order to treat that domain as a single layer. This approach is different than the one that I used in section 5.2 and 5.3 to calculate the thicknesses of this area which is the subdivision of the domain to smaller uniform layers of thickness equal to the maximum thickness found in the (z_{min}, z_{max}). In these test examples $a = 0.5$, $n = 10$, $z^c_{min} = 1$ and $z^c_{max} = 4$.

The acceptable models are defined by the χ^2 window which is set to $1 - 1.5$ for the cells in Northern Alpine foreland and Alpine Orogen crust, while for the case of South-West Alpine foreland I imposed it equal to $0.5 - 1$.

The sample cells chosen for this test are shown in figure 5.8 and represent four different types of crust: Northern Alpine foreland (C), South-West Alpine foreland (D) and Alpine Orogen Crust (E).

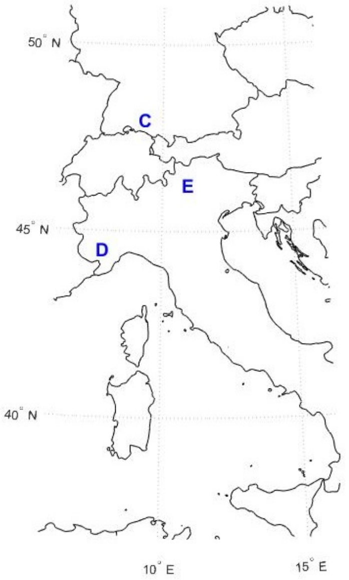

Figure 5.8: Sample cells in Nothern Alpine, that was made the pertubational and nonperturbational inversion.

I used the phase-velocity data constructed at each cell. Since the construction of the nonuniform computational grid is based on the data, for each cell the builded layered model is different and as such, in order to find an acceptable initial model, the type of inversion and the range of the correlation length and the model standard deviation factor has to be implemented differently for each case.

The parameters that need to be defined for the perturbational inversion, are the same as in section 5.2. The covariance matrices for the data and the model are calculated in the same manner and the inversion is made without maintaining fixed the Vp/Vs ratio. For the cases of Northern Alpine foreland and Alpine Orogen crust, the noise equals 1%, while for the case of South-West Alpine foreland equals 0.5%.

After testing for all three nonperturbational inversion ways (section 3.3) the data of each cell over different ranges of correlation length and of model standard deviation factor, and comparing the final update model from the perturbational inversion with the best model provided by Molinari et al. [2], I found the best choice of the aforementioned parameters.

For the case of the Northern Alpine foreland (point C in 5.8), the correlation length factor runs from 100 to 5000, while the model standard deviation factor from 0.3 to 0.7. The nonperturbational inversion is made by assuming the wave propagation on a different homogeneous medium, at each frequency, with a Poisson's ratio of 0.45. The χ^2 values for the models defined by the two ranges and which fit the data between the χ^2 window, are included between the two white dashed lines in figure 5.9 (a). In the same figure, I present the dispersion curves (b), the shear-wave velocity models (c) and the sensitivity kernel of the final inversion update (d). In order to evaluate both initial and final update models, I have included in the subfigures (b) and (c) the predicted data and the 1D vertical profile of the best model.

Although, I used the simplest case for the formulation of the Rayleigh-wave eigenfunctions, the initial model, although slow at the superficial layers, in general is close to the values of the best model and after the perturbational inversion, it is improved (figure 5.9 (c)). The depth resolution is between $4 - 15$ km (figure 5.9 (d)).

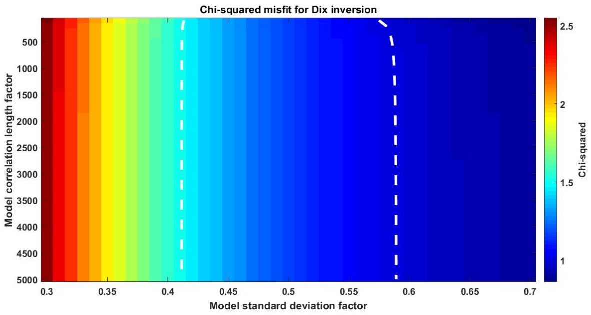

(a) χ^2 misfit the Dix-type phase inversion. The dashed white lines indicate the acceptable limits on chi-squared for models to be considered.

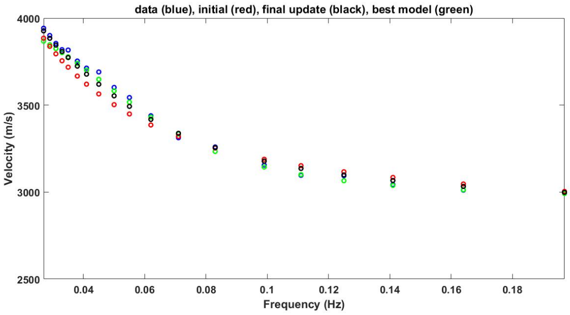

(b) Dispersion curves of the data(blue), the data from the Dix-initial model (red), the predicted data inversion (black) and the predicted data from the best-fitting model of Molinari et al. [2].

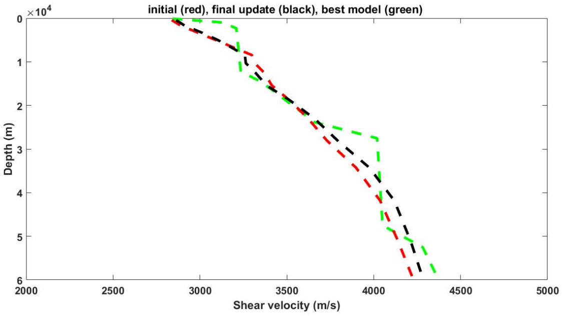

(c) Shear-wave velocity of the Dix-initial model (red), final update (black) and best-fitting model [2].

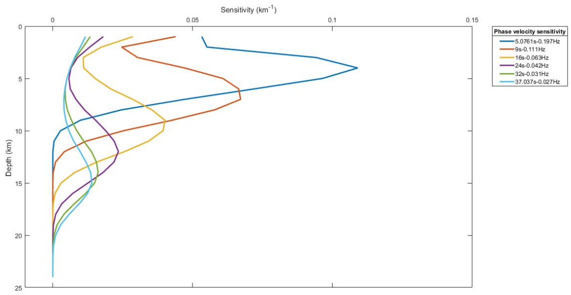

(d) Sensitivity Kernel of the final update for the periods of 5 s, 9 s, 16 s, 24 s, 32 s and 37 s.

Figure 5.9: Nothern Alpine foreland (C)

A similar approach is followed for the rest of the cases.

For the South-West Alpine foreland, the inversion for the research of an initial model is made by considering that the shear-wave velocity profile is described by a power law, with a Poisson's ratio equal to 0.3. The range over the correlation length factor is $100 - 2000$ and over the standard deviation factor $1 - 60$ (figure 5.10 (a)). Even in this case, at the superficial layers the initial and inverted models are slower than the best one(figure 5.10 (c) red dashed, black dashed and green dashed, respectively). The resolution depth, which is defined by the sensitivity of the Rayleigh velocity at a certain time to the variations of the shear-wave velocity at a certain depth, is between 4 and 15 km. We can observe that although the predicted data do not fit well the observed data for the high frequencies ($0.14 - 0.19$ Hz), convergence is found anyway and the iteration process stops when the data discrepancy produces a χ^2 value, that enters the predefined limits.

For the cell case in the Alpine Orogen crust, the range over the correlation length factor is from 100 to 5000 and over the model standard deviation factor $1 - 40$. Again, the power law shear velocity profile is used, with a Poisson's ratio of 0.25. Although in figure 5.11 (c), we can see that the nonperturbational inversion generates an initial model (red dashed) not so close to the best model for the same cell, after some updates of the perturbational inversion the resulting inverted model has the same velocity evolution as the best model, for the first 10 km. Below that depth (15 km), the initial model becomes slower, and so the final update of it, but at this depth there is poor resolution (figure 5.11 (d)).

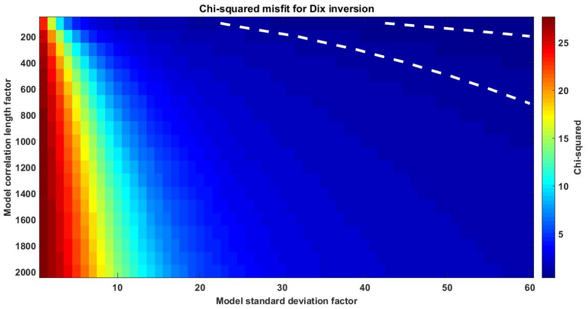

(a) χ^2 misfit the Dix-type phase inversion. The dashed white lines indicate the acceptable limits on χ^2 for models to be considered.

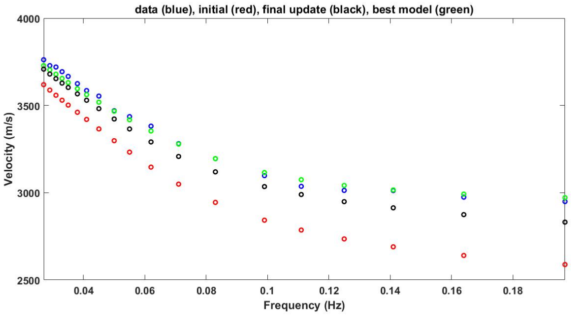

(b) Dispersion curves of the data(blue), the data from the Dix-initial model (red), the predicted data inversion (black) and the predicted data from the best-fitting model of Molinari et al. [2].

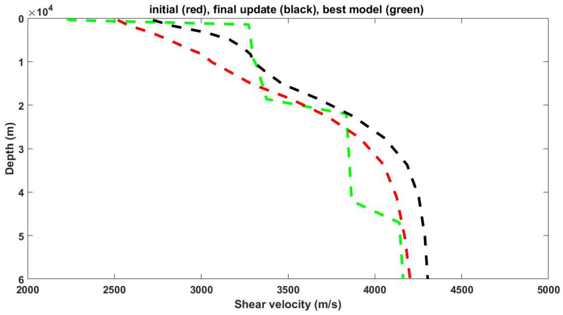

(c) Shear-wave velocity of the Dix-initial model (red), final update (black) and best-fitting model [2]

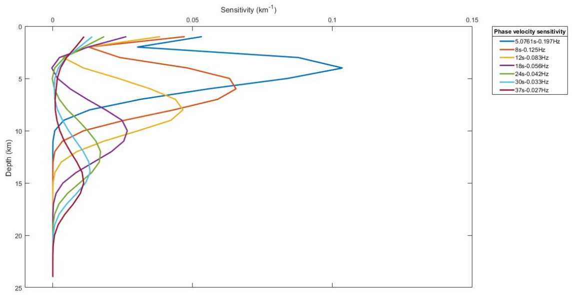

(d) Sensitivity Kernel of the final update for the periods of 5 s, 8 s, 12 s, 18 s, 24 s, 30 s and 37 s.

Figure 5.10: South-West Alpine foreland (D)

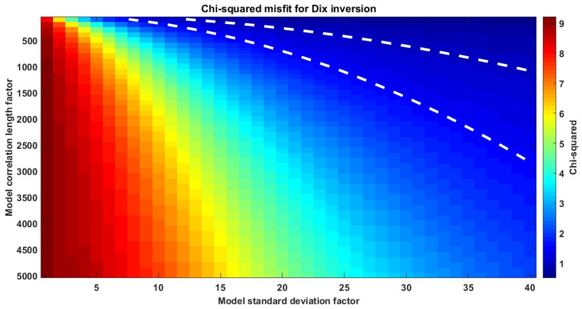

(a) χ^2 misfit the Dix-type phase inversion. The dashed white lines indicate the acceptable limits on χ^2 for models to be considered.

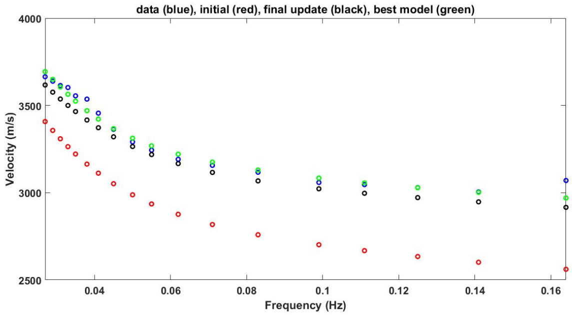

(b) Dispersion curves of the data(blue), the data from the Dix-initial model (red), the predicted data inversion (black) and the predicted data from the best-fitting model of Molinari et al. [2].

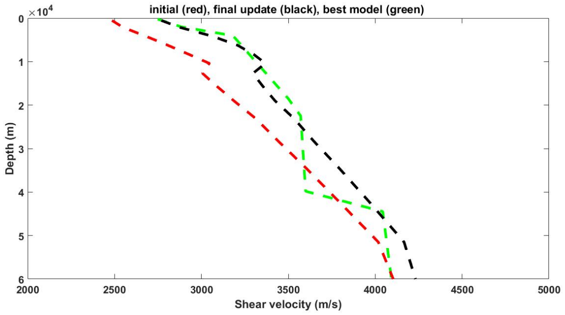

(c) Shear-wave velocity of the Dix-initial model (red), final update (black) and best-fitting model [2].

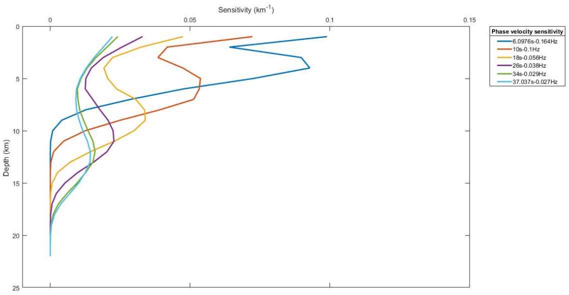

(d) Sensitivity Kernel of the final update for the periods of 6 s, 10 s, 18 s, 26 s, 34 s and 37 s.

Figure 5.11: Alpine Orogen crust(E)

Conclusion

The present thesis is based on the study of Rayleigh-waves and their particular property, the dispersion, which make a valuable tool to study the Earth subsurface. From the seismic records and after some elaboration, the dispersion curves (group and phase velocity as a function of frequency) are obtained: since Rayleigh waves are strongly affected by the elastic properties of the medium across which they have propagated, the dispersion data contain information relative to the structure. Inverting the dispersion curves with appropriate methods and procedures, it is possible to determine the shear-wave velocity structure of the medium.

In this particular work, and by following Haney and Tsai [1], two kinds of inversion are introduced. The perturbational approach, which is based on finite elements, and the nonperturbational approach, which is developed on the Dix formula for the calculation of the velocity values in a layered medium.

The first approach constitutes the iterative process used in order to improve an initial model. It is based on the perturbational theory, which relates the perturbations in the model parameters with the perturbations in the phase velocity. Practically, the forward and inverse problem are solved together: this happens because firstly from an initial model, phase-velocity data are predicted and then, the inversion procedure is looking for an appropriate model perturbation, until when the predicted dispersion curve fits well enough the observed one (data). In order to achieve accuracy, a certain number of iterations is needed.

In order to formulate the forward problem, the continuous system is represented by a stack of finite elements, whose corners are occupied by masses [6]. By considering the appropriate displacement and force vectors applied to these masses, the problem reduces to a simple eigenvalue/eigenvector problem to be solved by established numerical codes. The difference of the lumped mass method with the often used propagator matrix methods [14] is that there is no use of the displacement potentials, which leads to the seeking the roots of a polynomial.

With this solution of the forward problem, phase-velocity inversion proceeds using the algorithm of total inversion [7]. The solution is regularized on the basis of weighted-damped least squares.

This method is a linearised inversion and as such, a recovered model might bear some influence from the initial reference.

This is why, finding a good initial model remains an important task. Haney and Tsai [10] have found analogy between the relations of surface and shear-wave velocity and stacking and interval velocity, in flat, parallel layers. Consequently, based on the resulting direct relation between phase and shear-wave velocity, they have devised the nonperturbational inversion strategy.

At the beginning of the data analysis part, I solve the forward problem for specific initial models. Since the phase-velocity dispersion curve is in function of the Earth parameters (Vs, Vp, density), I apply to the initial model depth-dependent variations for every of the first three parameters, and observe the resulting perturbation in the dispersion curve.

The variation, that I implement to the parameters is a small increase from their initial value for three different depth domains. As expected, the variations in shear-wave velocity provide a dramatic effect on the Rayleigh-wave phase velocities. Variations in shallow layers affect the dispersion curve in the high-frequency range, while at lower frequencies the waves are more sensitive to deeper structure.

There is a resulting effect from the P-wave speed as well, especially at the high frequency band, but it is not comparable to the contribution of the S-wave speed to the data. However, sometimes inversion for the P-wave velocity might provide valuable information.

There is negligible effect from the variation of the density. In fact, most of the times this parameter is not even included in the inversion procedure.

Following, I implemented some synthetic test in order to better understand the sensitivity of the different parameters used in the inversion procedure. The tests were made for an arbitrary sample cell in oceanic crust. The initial model is taken from CRUST1.0 [9], while a target model has been created with elastic parameters close to the initial model. During the tests I considered variations in the frequency range, in the initial model and in the total thickness of the layered grid. In some of the cases the fundamental mode and first overtone phase velocity data are jointly inverted. In all of the tests the finite-element computational grid consists of layers with equal thickness, apart from the last one in which a nonuniform grid was used.

CRUST 1.0 is a global reference model with well-defined velocity differences between the assigned Earth layers. When such kind of initial model is implemented to a linearised method, like the one used in the present thesis, its final update will be affected by the discontinuities, and will mask any potential heterogeneity, that exists in the same depth domain, provided by the data. For this reason, I choose to implement an initial model which is a smooth representation of the boxcar form-like CRUST 1.0. Since the Moho is an important discontinuity, I explicitly add it to the tests.

An important finding of these tests was the importance of changing the regular computational grid to a nonuniform one and increasing the smoothness scale in depth. In this way, the Rayleigh-waves are well-sampled, which can be seen by the smaller computational times and the non-existence of instabilities in the resulting model. In order to well-represent any heterogeneity at the considered depth-domain, the smoothness scale should be in the same order of magnitude with depth.

Thanks to the findings of the synthetic tests, I was able to apply the whole inversion procedure to an already existing Rayleigh wave phase velocity database. This database was constructed by measuring the surface wave phase velocity obtained from the cross-correlation os seismic ambient noise [2]. The main results, in this case, is a 3D shear velocity model of the Alpine and the Italian crust, that can be compared to the one obtained by Molinari et al [2]. There are two distinct cases in terms of the a priori model.

In the first case, the a priori model that I use, is the crustal part of an average of the 500 best solutions obtained by the nonlinear inversion of Molinari et al. [2], and at the upper mantle part the PREM [3]. The 3D model presented in the third section of the Chapter 5 are mostly consistent with the equivalent maps of the aforementioned article.

The uppermost part of the crust together with the sediment basin are well-imaged at the 4 km map. The two basins in the north and the south of the Alps are evident, as it is part of the Ligurian oceanic crust. Although, in the work of Molinari et al. the Po Plain basin and Ligurian crust reveal lower velocities from the Northern Alpine basin, in the present work the two basins seem to have the same velocity, which is lower than the velocities in Ligurian crust. In the Po Plain basin the velocity is not uniformly distributed , which might be a clue of poor resolution or instability. The Alps and the Apennines, in both works have the same high velocity values ($\sim 3.2 - 3.5$ km/s). The differences in the shear-wave velocity indicate the different subsurface evolution.

In 10 km depth the difference in velocity between the Alps and its two basins is well-observed. The Po Plain basin seems to have lower velocities than the Northern Alpine foreland basin, which is an evidence of their different evolution. The Alps appears to have higher velocity values. The velocity range in the Tyrrhenian crust indicates that the Moho depth is reached, which seems to be reasonable when the oceanic crust is the case.

In the 20 km deep section, the velocity in the Alps is close to the value of 3.2 km/s, while in the south-east and south-west domains the velocities are higher. There is also a well-distinguished velocity difference between the high values of the Tuscan Apennines and low values of the Marche area. This velocity map is in accordance with the equivalent map in the work of Molinari et al. [2].

At around $30 - 35$ km depth, the shear-wave velocity values indicate that the Moho discontinuity has been reached for almost all the areas shown in the map: exception for the Alps and the Apennines, whose velocities $3.5 - 3.8$ km/s are consistent with the lower crust velocity values.

A vertical section of the shear velocity model is presented across the Eastern part of the Alps. The shear-wave velocity values of parts of the Apennines, the Po Plain basin, the Alps and the Northern Alpine Foreland are imaged vertical, and indicate clearly the Moho depth.

To conclude the work of this thesis, I repeated the inversion just described to a few sample cells, from the same database, using a different a priori model. This model is the result of a nonpertubational inversion based on the Dix-formula.

Since this model is based on the phase velocity measurements, it provides a potent solution in the choice of the a priori model, when the shear-wave velocity structure has to be found in areas with no a priori information.

This is in part true, because in the code the user has to provide some a priori information. The Poisson's ratio or the parameters needed for the calculation of the nonuniform computational grid must be supplied in order to proceed with the nonperturbational inversion.

This was demonstrated and presented in section 5.4. Tests over the user-supplied parameters were made in order to obtain a satisfying initial model. "Satisfying" in this work is defined the initial model which will be close to the already established best model from the work of Molinari et al. [2].

The three sample cells are representative of the Northern Alpine foreland, the Alpine Orogen crust and the South-West Alpine foreland.

Individually, there can be found a satisfying initial model for all of the cases, which with the perturbational inversion is further improved. It was challenging though, to find a unique set of parameters that will provide an acceptable initial model for all of the cases. It was even more difficult to apply the same nonperturbational inversion scheme in a wider area, like the Northern Italy. Whenever an acceptable model was not found over the specific parameters for a given cell, a gap was created in the 1D shear-wave velocity profile for that cell. In addition to this, there has to be found a compromise between runtime and search over the defined, by the user, parameter ranges for any potential solutions.

But even the perturbational inversion, which constitutes the main algorithm of this work, presents some salient points that need to be considered.

An important task was to define the computational grid. For the scope of this work, I have used two ways of determining the spacing on the finite-element layering. The first one is the uniform layering. The layers, whose sum represents the continuous system, are assigned with the same thickness. The second type of layering is the nonuniform one. In this case, the element thicknesses are defined on the basis of considerations made about the approximate depth domain where the Rayleigh waves reveal the maximum sensitivity.

There is one main advantage of using the second approach of layering over the first one. Since the sensitivity depth domain is calculated on the basis of phase velocity dispersion curves, the Rayleigh waves are properly sampled over both shallow and deep depth domains. This is why the computational grid contains thin layers in surface, which increase with increasing depth. With this proper sampling, instabilities are avoided and the computational times are shorter.

An other important issue was the determination of the smoothness scale. This parameter scales the size that any potential heterogeneity might obtain at the final inversion update. I made its calculation on the basis of the nonuniform optimal layering, and so it increases with increasing depth.

As already mentioned, in order to calculate the model standard deviation, I need to multiply the average of the data standard deviations with a user-supplied coefficient. This coefficient, which controls the size of the model standard deviation with respect to the size of the data standard deviations, should be kept near the values of $1 - 2$, otherwise provokes instabilities to the recovered model.

I have also implemented both of the two different ways to calculate the sensitivity kernel: either P-wave velocity and density fixed or Vp/Vs ratio and density fixed. The synthetic tests were realized with the second choice, while the inversion of the real dispersion curves with the first one. I found that with the second choice, and since the P-wave velocity equals the product of the S-wave velocity with the Vp/Vs ratio, restricts the recovered model, mainly in the low frequencies.

The most important factor for the execution of a linearised inversion, like the one that I used for the present work, is the a priori knowledge. Since the influence of the initial model to the recovered one is large, I must choose a good starting model which will be improved in a iterative way by the inversion procedure.

Appendix A:Stiffness Matrices

Kausel [16] showed that the elemental matrix associated to the N-th element is

$$\mathbf{M_N} = h_N \begin{bmatrix} \rho_N/3 & 0 & \rho_N/6 & 0 \\ 0 & \rho_N/3 & 0 & \rho_N/6 \\ \rho_N/6 & 0 & \rho_N/3 & 0 \\ 0 & \rho_N/6 & 0 & \rho_N/3 \end{bmatrix} \tag{5.1}$$

After the mass lumping (by Lysmer [6]) the matrix becomes

$$\mathbf{M_N^L} = h_N \begin{bmatrix} \rho_N/2 & 0 & 0 & 0 \\ 0 & \rho_N/2 & 0 & 0 \\ 0 & 0 & \rho_N/2 & 0 \\ 0 & 0 & 0 & \rho_N/2 \end{bmatrix} \tag{5.2}$$

The matrix $\mathbf{M}$ can be calculated in the same way as shown in figure 2.3. The rest of the matrices $\mathbf{B}_0$, $\mathbf{B}_1$, $\mathbf{B}_2$ are calculated similarly.

Bibliography

[1] M. M. Haney and V. C. Tsai, “Perturbational and nonperturbational inversion of rayleigh-wave velocities,” *GEOPHYSICS*, vol. 82, no. 3, pp. F15–F28, 2017.

[2] I. Molinari, J. Verbeke, L. Boschi, E. Kissling, and A. Morelli, “Italian and alpine three-dimensional crustal structure imaged by ambient-noise surface-wave dispersion,” *Geochemistry, Geophysics, Geosystems*, vol. 16, no. 12, pp. 4405–4421, 2015.

[3] A. Dziewonski and D. Anderson, “Preliminary reference earth model,” *Phys. Earth Plan. Int. 25:297-356*, 1981.

[4] `https://www.analog.com/en/analog-dialogue/articles/sensing-analyzing-and-acting-during-an-earthquake.html`.

[5] J. Xia, R. D. Miller, and C. B. Park, “Estimation of near-surface shear-wave velocity by inversion of rayleigh waves,” *GEOPHYSICS*, vol. 64, no. 3, pp. 691–700, 1999.

[6] J. Lysmer, “Lumped mass method for rayleigh waves,” *Bulletin of the Seismological Society of America*, vol. 60, no. 1, p. 89, 1970.

[7] A. Tarantola and B. Valette, “Generalized nonlinear inverse problems solved using the least squares criterion,” *Reviews of Geophysics*, vol. 20, no. 2, pp. 219–232, 1982.

[8] E. Muyzert, “Seabed property estimation from ambient-noise recordings: Part 2 — scholte-wave spectral-ratio inversion,” *GEOPHYSICS*, vol. 72, no. 4, pp. U47–U53, 2007.

[9] `https://igppweb.ucsd.edu/~gabi/rem.html`.

[10] M. M. Haney and V. C. Tsai, “Nonperturbational surface-wave inversion: A dix-type relation for surface waves,” *GEOPHYSICS*, vol. 80, no. 6, pp. EN167–EN177, 2015.

[11] C. Fowler, C. Fowler, and C. Fowler, *The Solid Earth: An Introduction to Global Geophysics*, ch. 4. Cambridge University Press, 2005.

[12] S. Stein and M. Wysession, *Introduction to Seismology, Earthquakes, and Earth Structure.* Blackwell Publishing, 2003.

[13] O. Novotný, *Seismic Surface Waves.* 1999.

[14] H. Takeuchi and M. Saito, "Seismic surface waves," in *Seismology: Surface Waves and Earth Oscillations* (B. A. BOLT, ed.), vol. 11 of *Methods in Computational Physics: Advances in Research and Applications*, pp. 217 – 295, Elsevier, 1972.

[15] K. Aki and P. G. Richards, *Quantitative Seismology, 2nd Ed.* University Science Books, 2002.

[16] E. Kausel, *Waves Propagation Modes: From Simple Systems to Layered Soils*, pp. 165–202. Vienna: Springer Vienna, 2005.

[17] G. Nolet, R. Sleeman, V. Nijhof, and B. L. N. Kennett, "Synthetic reflection seismograms in three dimensions by a locked-mode approximation," *GEOPHYSICS*, vol. 54, no. 3, pp. 350–358, 1989.

[18] A. Tarantola, *1. The General Discrete Inverse Problem*, ch. 1, pp. 1–40.

[19] W. L. Rodi, P. Glover, T. M. C. Li, and S. S. Alexander, "A fast, accurate method for computing group-velocity partial derivatives for rayleigh and love modes," *Bulletin of the Seismological Society of America*, vol. 65, no. 5, pp. 1105–1114, 1975.

[20] W. Menke, *Geophysical Data Analysis: Discrete Inverse Theory: MATLAB Edition.* International Geophysics, Elsevier Science, 2012.

[21] R. Richardson and G. Zandt, *Inverse Problems in Geophysics GEOS 567.* 2003.

[22] `https://software.seg.org/GEOindex.html`.

[23] P. Gerstoft, K. G. Sabra, P. Roux, W. A. Kuperman, and M. C. Fehler, "Green's functions extraction and surface-wave tomography from microseisms in southern california," *GEOPHYSICS*, vol. 71, no. 4, pp. SI23–SI31, 2006.

[24] I. Molinari, "Potere risolutivo delle onde sismiche superficiali in presenza di anisotropia radiale," Master's thesis, Università di Bologna, 2007.

[25] G. H. F. Gardner, "Formation velocity and densitythe diagnostic basics for stratigraphic traps," *Geophysics*, vol. 39, p. 770, dec 1974.

[26] L. Stehly, M. Campillo, and N. M. Shapiro, "A study of the seismic noise from its long-range correlation properties," *Journal of Geophysical Research: Solid Earth*, vol. 111, no. B10, 2006.

[27] Y. Yang and M. H. Ritzwoller, "Characteristics of ambient seismic noise as a source for surface wave tomography," *Geochemistry, Geophysics, Geosystems*, vol. 9, no. 2, 2008.

[28] M. Sambridge, "Geophysical inversion with a neighbourhood algorithm—i. searching a parameter space," *Geophysical Journal International*, vol. 138, no. 2, pp. 479–494, 1999.

[29] M. Sambridge, “Geophysical inversion with a neighbourhood algorithm—ii. appraising the ensemble,” *Geophysical Journal International*, vol. 138, no. 3, pp. 727–746, 1999.